

Manuscript version: Author's Accepted Manuscript

The version presented in WRAP is the author's accepted manuscript and may differ from the published version or Version of Record.

Persistent WRAP URL:

<http://wrap.warwick.ac.uk/156118>

How to cite:

Please refer to published version for the most recent bibliographic citation information. If a published version is known of, the repository item page linked to above, will contain details on accessing it.

Copyright and reuse:

The Warwick Research Archive Portal (WRAP) makes this work by researchers of the University of Warwick available open access under the following conditions.

© 2021 Elsevier. Licensed under the Creative Commons Attribution-NonCommercial-NoDerivatives 4.0 International <http://creativecommons.org/licenses/by-nc-nd/4.0/>.



Publisher's statement:

Please refer to the repository item page, publisher's statement section, for further information.

For more information, please contact the WRAP Team at: wrap@warwick.ac.uk.

1 **Effect of coiling temperature on impact toughness of hot rolled**
2 **ultra-high-strength multiphase steel strips**

4 **Abhisek Mandal^{1*}, Abhijit Ghosh², Debalay Chakrabarti¹ and Claire Davis³**

6 ¹*Department of Metallurgical and Materials Engineering, IIT Kharagpur, Kharagpur 721302, India*

7 ²*Department of Metallurgical and Materials Engineering, IIT Indore*

8 ³*Warwick Manufacturing Group, University of Warwick, Zip-CV4 7AL, England, UK*

10 *Corresponding Author, Mailing ID: abhisekm9@gmail.com,

12 **ABSTRACT**

14 The tensile and Charpy impact properties of four strip samples from two different B-added
15 low-C ultra-high-strength steel strips (Al-treated and Ti-treated), coiled at two different
16 temperature ranges (360-380°C and 450-460°C), have been evaluated and correlated to the
17 microstructural parameters, dislocation density, and the intensity of high-angle boundaries. The
18 effects of coiling temperatures on the microstructural evolution and mechanical properties have
19 been discussed. The volume fraction of the individual phase constituents (namely, granular
20 bainite, upper bainite, lower bainite and tempered martensite) and their hardness, local
21 deformation response and the strain-hardening ability, as determined from nanoindentation
22 testing, influenced the bulk properties such as hardness, tensile properties (strength and
23 ductility), Charpy impact properties (upper shelf energy, USE, and ductile-to-brittle transition
24 temperature, DBTT) and strain-hardening abilities under both quasi-static and dynamic loading
25 conditions. The dominance of granular bainite and upper bainite (75-90%) reduced the strength
26 (670-722 MPa yield strength), improved ductility (16.7 – 19.5% elongation to failure) and USE
27 (35-42 J) in the samples coiled at the higher temperatures. In contrast, a higher fraction of
28 tempered martensite and lower bainite (78-82%) significantly increased the strength (808-814
29 MPa), reduced ductility (13.0-14.5%) and USE (19-29 J) in the lower temperature coiled
30 samples. The DBTT showed a complex trend with the microstructural parameters. It depended
31 on the USE level, as well as on the ‘effective grain size’ of the matrix.

32 **Keywords:** Ultra-high-strength steel; Coiling temperature; Bainite-martensite microstructure;
33 Strain-hardening; Charpy impact testing; Upper shelf energy; Ductile-brittle transition
34 temperature.

36 **1. Introduction**

37 There has been an increasing interest to develop ultrahigh-strength steels (UHSS) with
38 a yield strength greater than 700 MPa, for various applications, such as construction,
39 transportation, engineering, shipbuilding, energy, and defence [1]. Such a development is
40 driven by the requirement of light-weight structures to achieve significant cost and energy

41 savings (through reduced requirement of material and welding consumables), easy
42 transportation, and even improved toughness (due to the reduced section thickness) ensuring
43 structural integrity [1].

44 Regarding the standard specifications for structural steels, an excellent combination of
45 strength, ductility, and impact toughness is an essential requirement [2,3]. Regarding
46 thermomechanically processed and controlled cooled high-strength strip steels, the role of
47 processing parameters such as soaking temperature, start- and finish-rolling temperatures,
48 rolling reduction ratio, cooling start- and end temperatures and cooling rate on the
49 microstructure and mechanical properties have been studied extensively [4–6]. It is noteworthy
50 that UHSS strips (< 10 mm thickness) are usually coiled after finish rolling, and use accelerated
51 cooling to a lower temperature range (typically, 350 - 460 °C) to achieve high strength by the
52 formation of bainite-martensite mixed microstructures [7–13]. An increase in strength,
53 however, is often accompanied by a decrease in ductility and impact toughness [14]. Although
54 a bainite-martensite microstructure can achieve sufficient strength [15–18], regarding impact
55 toughness, it faces a strong challenge from other microstructures such as complete tempered
56 martensite, acicular ferrite, ultrafine-grained ferrite, or a complex combination of different
57 constituents, including retained austenite [17–21]. Overall, the effects of coiling temperatures
58 on the microstructure and resultant tensile and Charpy impact properties of UHSS have hardly
59 been studied.

60 There has been a recent research interest to relate the micro-scale deformation
61 behaviour of the individual phase constituents to the tensile properties of multiphase steels [22–
62 28]. However, none of those studies extended that approach to explaining the impact toughness.
63 The effects of multiphase microstructures on the Charpy impact properties have been studied
64 separately [29–37]. Considering the role of bainite on ductility and impact toughness of bainite-
65 martensite steels, several conflicting observations have been reported. In general, the presence
66 of granular bainite or upper bainite imposes an adverse effect on the toughness of tempered
67 martensitic steels due to the following reasons: (i) The coarse carbide particles or coarse islands
68 of MA constituents act as cleavage crack initiation sites; (ii) The low-angle boundaries between
69 adjacent bainite laths (or sub-units) are ineffective in retarding (or deviating) cleavage crack
70 propagation; and (iii) Bainite is far less responsive to tempering (or coiling) treatment than
71 martensite [29–46]. Due to the finer carbide size as well as finer bainitic-ferrite plate, block,
72 and packet sizes, the impact toughness of lower-bainite is superior to that of granular- and
73 upper bainite [46]. On the other side, the presence of a limited amount of bainite (up to around
74 25 percent) along with martensite [47,48], a combination of ductile-bainite and carbon-depleted
75 martensite [5], or even a refined granular bainite microstructure [49–52] have been reported to
76 achieve high ductility and impact toughness. Overall, a refinement in prior-austenite grain size,
77 bainite packet size, as well as carbide particle size (or the MA constituent size) has been found
78 to improve the impact toughness [29–55]

79 In a recent review, Raabe et al. [29] emphasized the need for careful microstructural
 80 design for high strength steels avoiding the microstructurally supported crack initiation sites
 81 (say, hard martensite regions and carbide particles) and crack propagation sites (say, interfaces
 82 between hard and soft constituents). However, such a microstructural design cannot be fulfilled
 83 without a thorough understanding of the effect of individual microstructural constituents on
 84 properties such as strain-hardening, USE, DBTT, and fracture mechanisms of bainite-
 85 martensite UHSS under quasi-static tensile deformation as well as dynamic impact loading
 86 conditions. That is the objective of our paper. In a recent article [11], we have reported the
 87 effect of coiling temperatures on the microstructural evolution and the bending performance of
 88 two different B-containing structural grades of steels (one treated with Ti and the other treated
 89 with Al). The present study correlates the microstructural parameters with the tensile and
 90 Charpy impact properties of those multiphase UHSS strips.
 91

92 2. Materials and experimental details

93 Four samples with dimensions of 600 mm length, 300 mm width, and 6-8 mm thickness
 94 were received from Tata Steel Europe and were taken from boron-containing ultrahigh strength
 95 microalloyed steel strips. These steel strips were produced in industrial trials at Tata Steel and
 96 were part of a larger development program of UHSS intended to determine the optimal
 97 combination of chemical composition and processing parameters. To retain boron in solution
 98 by avoiding BN formation, it is necessary to treat the steel with a stronger nitride former, such
 99 as Ti or Al. The investigated steels were either Al-treated or Ti-treated and their chemical
 100 compositions are given in **Table 1**.

101 The strips were controlled rolled, with finish rolling temperatures of around 950 °C,
 102 accelerated cooled and coiled at two different temperature ranges; higher (450 °C to 460 °C)
 103 and lower (360 °C to 380 °C) coiling start temperatures. The schematic diagram of the
 104 thermomechanical processing is given in **Fig. 1**. The bainite and martensite transformation
 105 temperatures (predicted from JMatPro® software) for both the steel compositions are
 106 mentioned in **Fig. 1**. The steel samples were coded by the treatment adopted (Al- or Ti-)
 107 followed by the respective coiling start temperature, i.e., Al-450, Al-360, Ti-460, and Ti-380.
 108

109 Table 1: Chemical composition of the investigated steels (in wt. %).

Steel	C	Mn	S+P	Si	Al	Ti	Cu + Ni	Cr	Nb + Mo + V	B	N
Al-treated	0.117	1.571	0.014	0.057	0.068	0.003	0.030	0.503	0.322	0.0019	0.0046
Ti-treated	0.119	1.595	0.017	0.047	0.029	0.028	0.038	0.502	0.323	0.0019	0.0055

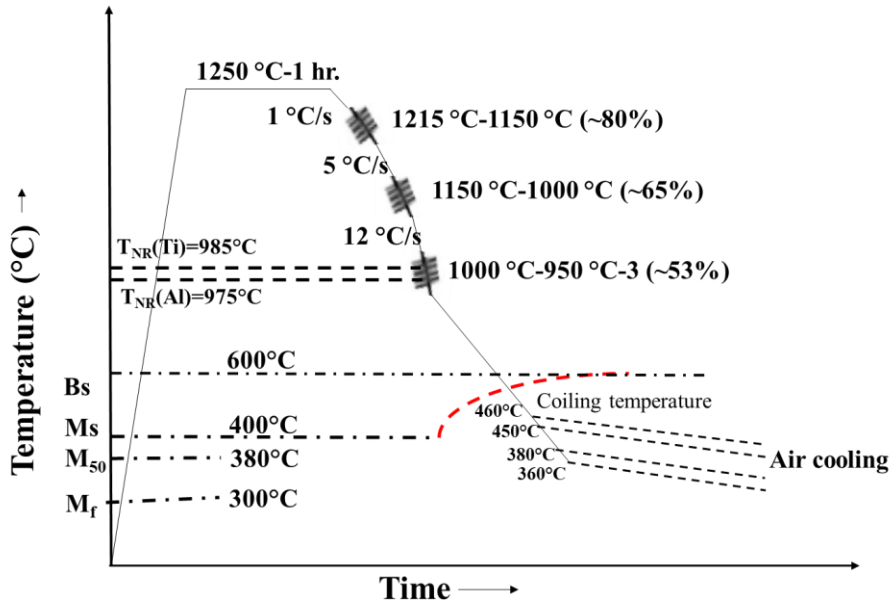


Fig. 1: Schematic diagram of the thermomechanical processing schedule applied on the investigated steel strips. Abbreviations: T_{NR}: Recrystallization stop temperature; B_s: Bainite transformation start temperature; B_f: Bainite transformation finish temperature; M₅₀: Temperature corresponding to 50% martensite transformation.

The following equation proposed by Boratto et al. [56] was used to predicted the recrystallization stop temperatures (T_{NR}) of the Al-treated and Ti-treated steels to be ~ 975 °C and ~ 985 °C, respectively.

$$T_{NR} = 887 + 464C + 890Ti + 363Al - 357Si + (644Nb - 644\sqrt{Nb}) + (732V - 230\sqrt{V}) \quad (1)$$

Thermodynamic calculations were accomplished using Thermo-Calc® 4.1 software based on the TCFE6 database considering the nominal steel compositions to forecast the formation of different phases and precipitates under equilibrium cooling. Cross-section planes (Rolling Direction, RD – Normal Direction, ND) of the samples were prepared following standard metallographic techniques, etched in 2 percent Nital solution, and investigated by optical microscopy (model-Leica DM600M) with the attachment of image analysis, and scanning electron microscopy (SEM model Zeiss EVO 60), with the attachment of energy dispersive spectroscopy (EDS). The microstructural study by SEM was carried out primarily at the quarter-thickness locations of the strip samples covering at least 500 μm × 500 μm area. Microstructural constituents such as granular bainite (GB), upper bainite (UB), lower bainite (LB), and tempered martensite (TM) were identified separately in high magnification (3000×) SEM images and their fractions were determined by image analysis (assuming estimated area percentage as volume percentage). Thin foils (~ 30 nm) were prepared by electropolishing using a solution of 80 percent methanol and 20 percent perchloric acid. These foils were studied by a high-resolution transmission electron microscope, TEM (JEOL-2000 FX, Japan).

136 Specimens for electron backscattered diffraction (EBSD) analysis were prepared by
137 mechanical polishing, followed by electropolishing at 20 V for 15 s using an electrolyte
138 containing 80 volume percent methanol and 20 volume percent perchloric acid. The EBSD
139 scans were performed at the quarter-thickness location at a step size of 0.1 μm using an Oxford
140 HKL Channel 5 system (Oxford Instruments, Oxfordshire, UK) attached to a Zeiss® Auriga
141 compact SEM with more than 95 percent accuracy of indexing. Considering the angular
142 resolution of EBSD, a minimum misorientation threshold of 2° was set for the analysis. The
143 boundaries between 2° and 15° misorientation and the boundaries greater than 15°
144 misorientation are identified as low-angle boundaries (LAB), i.e., ‘sub-boundaries’, and high-
145 angle boundaries (HAB), i.e., ‘grain boundaries’, respectively. XRD analysis was performed in
146 the Bruker D8 Discover model for quantification of the dislocation density in the samples.
147 Carefully prepared samples (gently polished) were used to avoid any contamination or strain
148 arising from grinding. The Co-K α radiation (wavelength: 1.789 Å) was selected as the incident
149 X-ray. Each sample was scanned over a 2 θ range of 45–120° with a step size of 0.02° and 2 s
150 time-per-step. According to the standard specification **BS EN 10025** [57] for UHSS, test
151 specimens were collected from the quarter-thickness location.

152 Vickers hardness readings were taken (based on the average of 10 readings for each
153 strip sample) at the quarter-thickness location on the RD-ND plane at 20 Kgf load with 15 s
154 dwell time using the LV-700 model LECO® hardness tester. Due to the very small indent size
155 ($\leq 1 \mu\text{m}$), nano-indentation testing was performed (on conventionally polished and lightly
156 etched specimens) to relate the local deformation response of individual phase constituents
157 with the mechanical properties. The tests were conducted at the quarter-thickness location of
158 the strips using Anton Paar GmbH Nanoindenter® (Santner Foundation, Austria) with a
159 Berkovich tip made of industrial diamond having an elastic modulus of 865 GPa and Poisson’s
160 ratio of 0.07. The continuous stiffness measurement (CSM) mode was used for the nano-
161 indentation measurements. The maximum load for testing was 10 mN with a linear
162 loading/unloading rate of 20 mN/min and 10 s dwelling time with a data acquisition rate of 10
163 Hz. A small load was used to confine the plastic zone of the indentation within that particular
164 microstructural constituent on which the hardness was meant to be probed. The nano-
165 indentation results for each sample were analyzed using Indentation 7.3.10 software® based
166 on 10 grids, each covering 5×8 indentations separated by a linear spacing of 10 μm .
167 Tensile specimens (**Fig. 2a**) were prepared following ASTM E8 standard [58] and tested in a
168 250-ton Universal Testing Machine Instron®8801 at room temperature ($\sim 25^\circ\text{C}$) and a strain
169 rate of $6.6 \times 10^{-4}/\text{s}$. A minimum of three tensile tests was carried out on each steel to ensure
170 repeatability. Standard sub-size V-notched Charpy specimens of the same dimension (**Fig. 2b**)
171 were prepared in the transverse-longitudinal (T-L) orientation with respect to the rolled plate
172 following ASTM E23 [59]. For tensile and Charpy impact testing 5 mm thick specimens were

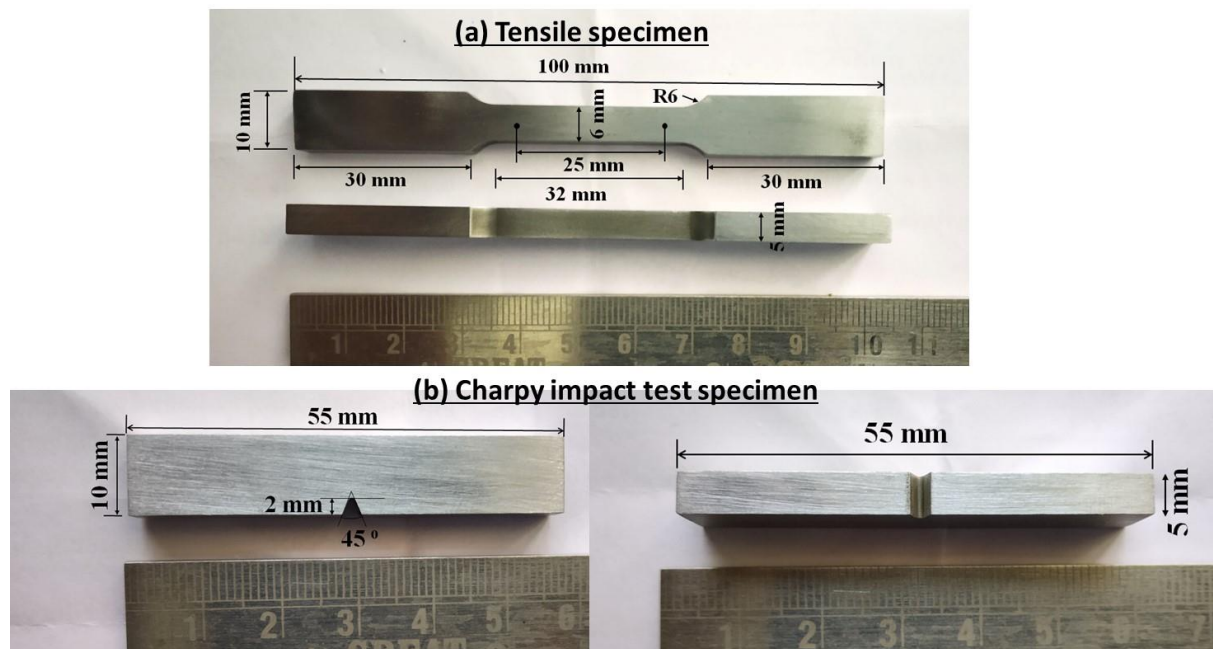
173 used. The 5 mm samples were extracted by machining off top and bottom of the strips,
174 i.e., covering the entire portion of the strips.

175 Charpy specimens were tested using an Instron® SI-1C3 model instrumental impact
176 testing machine (400J capacity), attached with Instron Dynatup Impulse data acquisition
177 system, over the temperature range of -193 °C to +70 °C. The specimen temperature was
178 continuously monitored by a thermocouple and was maintained within ± 2 °C using a medium
179 of methanol and liquid nitrogen. The Charpy impact transition curves were plotted within the
180 scattered data points of Charpy impact energy vs. test temperature by fitting a ‘tanh’ function
181 as given below [60]:

182
$$E_{CVN} = A + B \tanh\left(\frac{T-T_{DBTT}}{C}\right) \quad (2)$$

183 where, A, B, and C are constants, E_{CVN} stands for impact energy absorbed, T is test temperature
184 and T_{DBTT} is ductile-to-brittle transition temperature. A detailed fractography study has been
185 carried out on the broken Charpy impact specimens under SEM. Not only the fractographic
186 features on the fracture surfaces but also the defects on the transverse planes (prepared
187 metallographically and lightly etched with Nital) perpendicular to the main fracture surfaces of
188 the broken halves of Charpy specimens were examined.

189



190
191 **Fig. 2: Photographs of (a) tensile and (2) Charpy impact test specimens (Dimensions in
192 mm) used in the present study.**

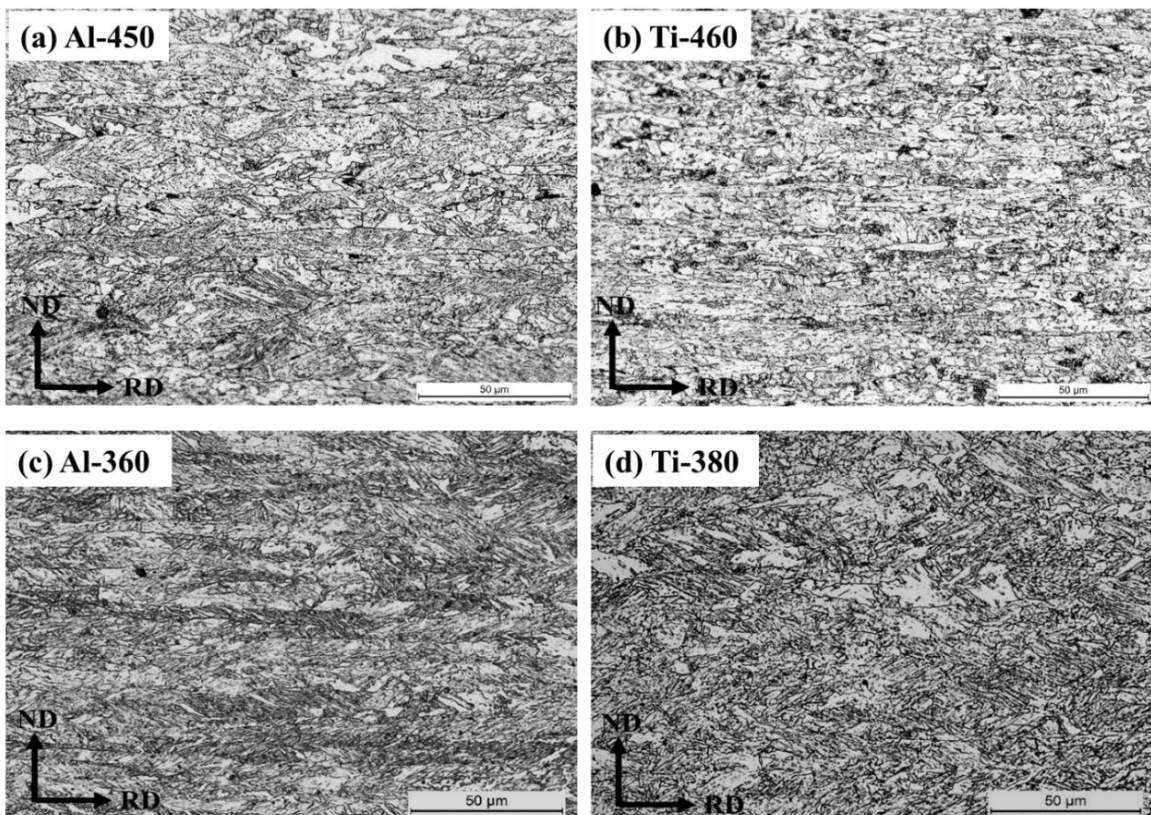
193

194 **3. Results**

195 **3.1. Microstructural characterization**

196 The optical micrographs and scanning electron micrographs taken from the RD-ND
197 plane of the rolled and coiled samples at the quarter thickness location are presented in **Fig. 3**

198 and **Fig. 4**, respectively. The micrographs show an elongated grain structure towards the rolling
 199 direction. The microstructure consisted of different forms of bainite, i.e., granular bainite (GB),
 200 upper bainite (UB), and lower bainite (LB) along with tempered martensite (TM) in some
 201 samples. High-magnification SEM images of the individual microstructural constituents are
 202 shown in **Fig. 4e**. Microstructural constituents are identified considering their morphological
 203 characteristic as reported in the literature [46] and also shown in our recent study [11].
 204



205
 206 **Fig. 3: Optical micrographs of the investigated samples taken from the RD-ND plane at**
 207 **quarter thickness locations. Sample codes are mentioned in the images.**

208
 209 The microstructural constituents can be divided into two major categories, softer
 210 constituents (GB and UB) and harder constituents (LB and TM). Volume fractions of the
 211 microstructural constituents in the investigated samples are listed in **Table 2**. The amounts of
 212 GB and UB were higher (75-90 percent) in Al-450 and Ti-460 samples coiled at the upper part
 213 of the bainitic transformation bay, i.e., below B_s (~ 600 °C) but above M_s (~ 400 °C). The GB
 214 and UB fractions were low (17-23%) in Al-360 and Ti-380 samples coiled below M_s . In
 215 contrast, a significant amount of TM (48-58 percent) was present in Al-360 and Ti-380 (coiled
 216 below M_s), whilst no evidence of TM was found in Al-450 and Ti-460 (coiled above M_s). The
 217 LB fraction was minimum in Ti-460, while it remained within a close range in the other
 218 samples (24 to 30 vol. percent).
 219

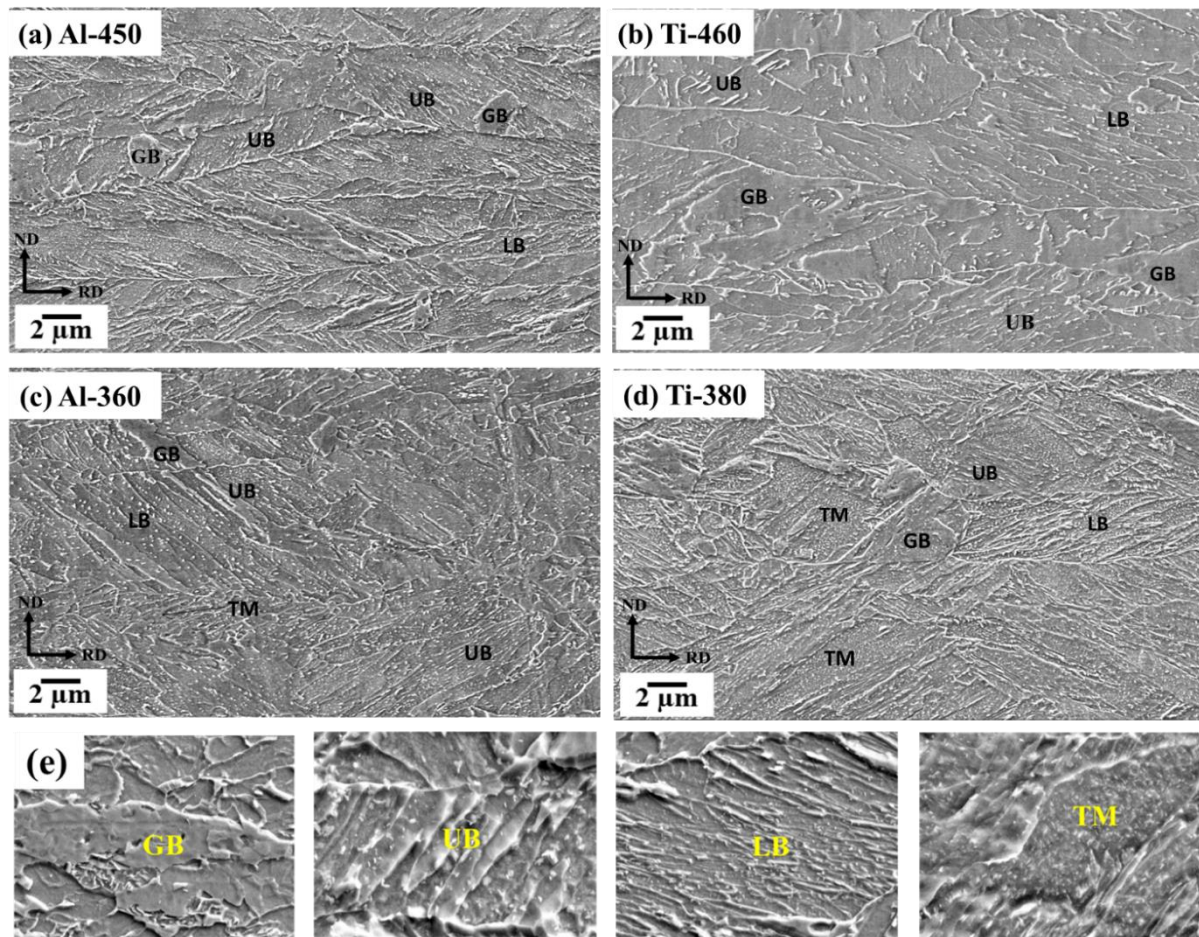


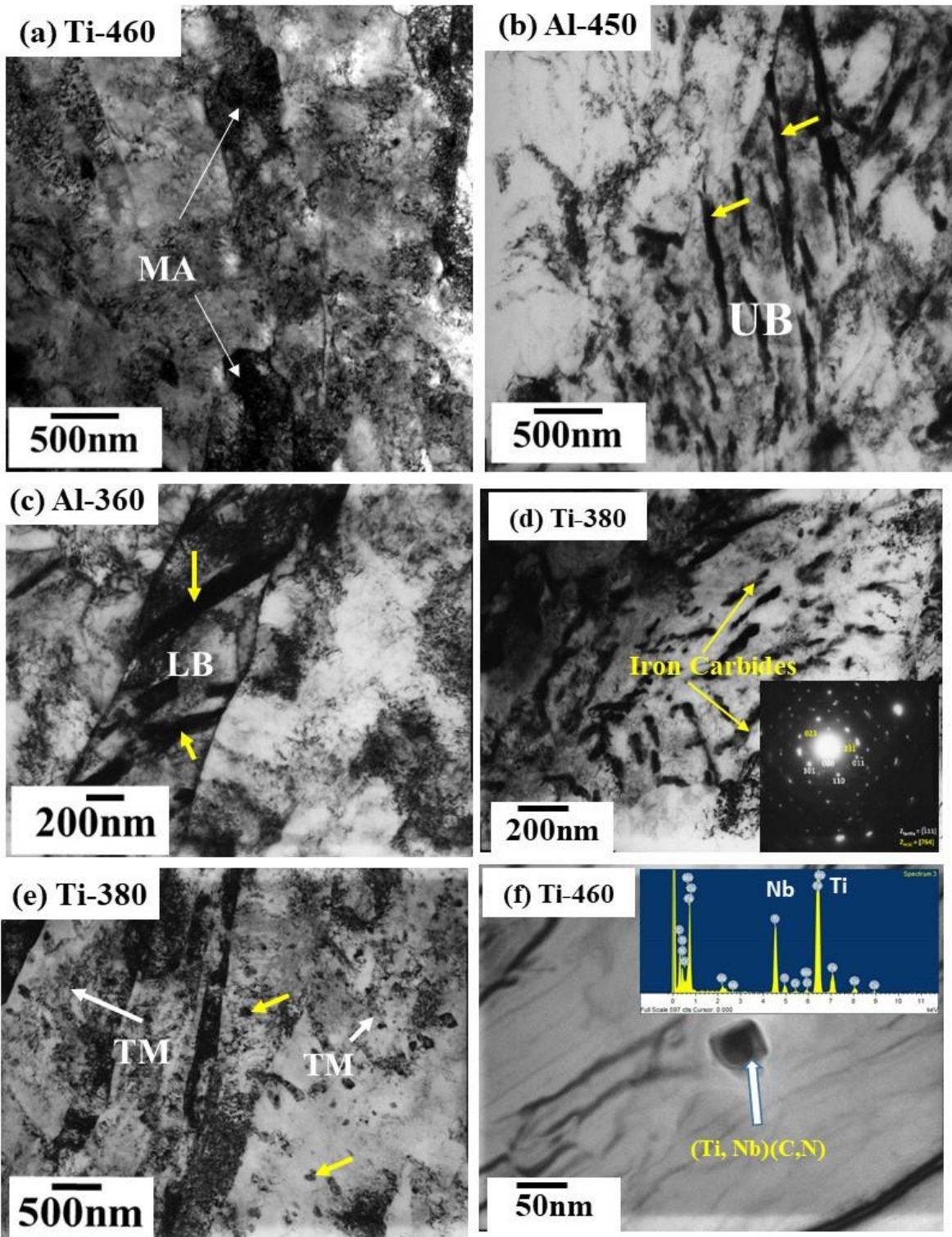
Fig. 4: (a-d) Scanning electron micrographs (secondary electron images) of the RD-ND plane of the investigated samples at the quarter-thickness location; (e) Higher magnification images of the individual phase constituents. Abbreviations: GB: Granular bainite, UB: Upper bainite, LB: Lower bainite, and TM: Tempered martensite. (a-d) Sample codes are mentioned in the images.

Table 2: Volume percentage of different microstructural constituents in rolled and coiled strips as measured by image analysis on SEM images.

Sample Code	Coiling Temperature (°C)	Softer constituents		Harder constituents	
		GB (vol. %)	UB (vol. %)	LB (vol. %)	TM (vol. %)
Al - 450	450	16 ± 4	59 ± 7	25 ± 2	-----
Al - 360	360	5 ± 2	13 ± 3	24 ± 3	58 ± 2
Ti - 460	460	25 ± 6	65 ± 5	10 ± 3	-----
Ti - 380	380	10 ± 2	12 ± 3	30 ± 2	48 ± 4

The intricate microstructural details can be identified from the TEM images in Fig. 5. The MA constituents within granular bainite in Ti-460 are indicated in Fig. 5a. The interlath

232 carbides at the upper bainite region in Al-450 are shown in **Fig. 5b**. Fine laths of lower bainite
233 with small carbide particles in Al-360 and Ti-380 are pointed in **Fig. 5(c and d)**. The selected
234 area electron diffraction (SAED) pattern inserted in **Fig. 5d** identifies the orthorhombic crystal
235 structure of cementite. Since the samples cooled slowly over a long duration during coiling
236 treatment, the epsilon-carbides converted to stable cementite particles. **Fig. 5e** also display the
237 fine cementite particles (arrowed) inside the tempered martensite laths in Ti-380. Coarse
238 cuboidal (Ti, Nb)(C, N) precipitates having a long diagonal length in the range of ~30 - 50 nm
239 were present in both Al- and Ti-treated steels, **Fig. 5f**. These coarse and brittle precipitates
240 could be the potential sites for cleavage crack initiation [61]. Detailed discussion on the
241 evolution of microstructure and precipitation during the casting, rolling and final coiling
242 treatment of the investigated strip samples are available in our earlier study [11].

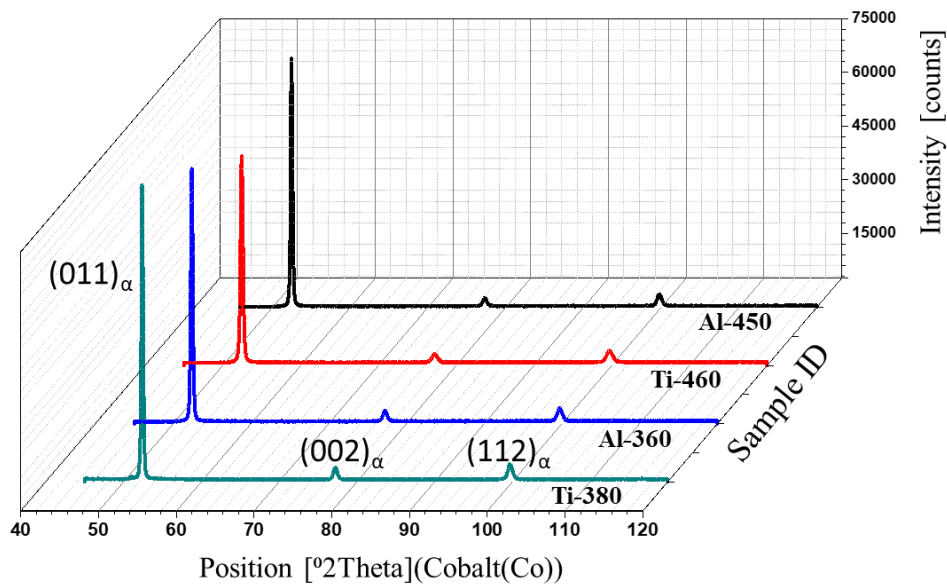


243
244 Fig. 5: (a-d) Bright-field TEM images showing characteristic microstructural features:
245 (a) Granular bainite with MA constituents (arrowed); (b) Upper bainite; (c and d)
246 Lower bainite; (e) Tempered martensite; and (f) A $(\text{Ti}, \text{Nb})(\text{C}, \text{N})$ precipitate (EDS
247 analysis inserted). The iron-carbide particles are indicated by yellow arrows.
248 SAED pattern inserted in (d) confirmed the presence of cementite. The specimen
249 codes are mentioned in the images.

250

251 **3.2. Estimation of dislocation density, lattice-strain, and grain boundary**
 252 **misorientation**

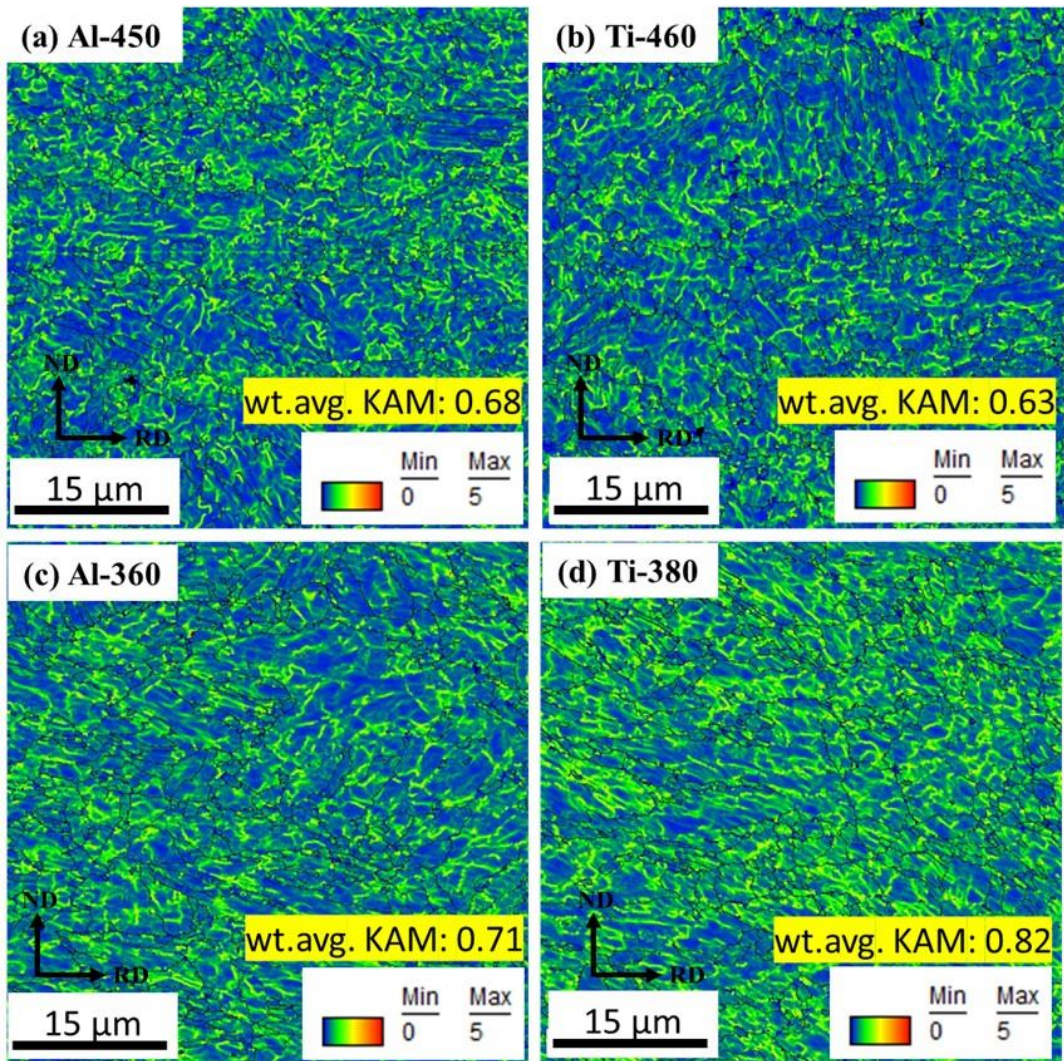
253 The dislocation densities at the quarter-thickness location of the rolled and coiled
 254 samples were calculated by profile analysis of the X-ray diffraction data, following the
 255 modified Williamson-Hall and Warren-Averbach methods [62,63]. X-ray diffraction plots of
 256 the investigated samples are shown in **Fig. 6**. **Fig. 6** shows the (011), (002) and (112) peaks
 257 corresponding to the BCC crystal structure. The dislocation density is calculated using the
 258 equation given in reference [64,65]. The dislocation densities increased in the following
 259 order, Ti-460 ($4.8 \times 10^{14} \text{ m}^{-2}$) < Al-450 ($6.9 \times 10^{14} \text{ m}^{-2}$) < Al-360 ($9.1 \times 10^{14} \text{ m}^{-2}$) < Ti-380
 260 ($14.0 \times 10^{14} \text{ m}^{-2}$). The lattice-strain distribution at a microscopic scale was estimated from the
 261 EBSD analysis and represented as Kernel Average Misorientation (KAM) maps in **Fig. 7**. The
 262 KAM represents the average misorientation angle of a given point, concerning its nearest
 263 neighbours, and it is directly related to the density of geometrically necessary dislocations
 264 [66,67]. The weighted average KAM values as stated on the respective KAM maps in **Fig. 7**,
 265 increased in the same order as the dislocation density (calculated from XRD), i.e., Ti-460 < Al-
 266 450 < Al-360 < Ti-380.



267
 268 **Fig. 6: X-ray diffraction plots of the as-received samples at room temperature.**

269 The boundary misorientation maps as obtained from the EBSD analysis are presented
 270 in **Fig. 8(a-d)**. The absolute frequency of occurrence of the boundaries (number/ μm^2)
 271 depending on the misorientation angles is plotted in **Fig. 8e**. The intensities of high-angle
 272 boundaries (HABs) were maximum in Ti-380, followed by Al-360, Al-450, and Ti-460. The
 273 intensities of low-angle boundaries (LABs) followed almost a similar trend. Thus, in low-
 274 temperature coiled samples (Ti-380 followed by Al-360), not only is the dislocation density
 275 high, but the absolute intensities of LABs and HABs were also high. Phase transformation at

276 lower coiling temperature resulted in higher dislocation density and the recovery of those
 277 dislocations (during coiling treatment) increased the intensity of LABs [46][68].

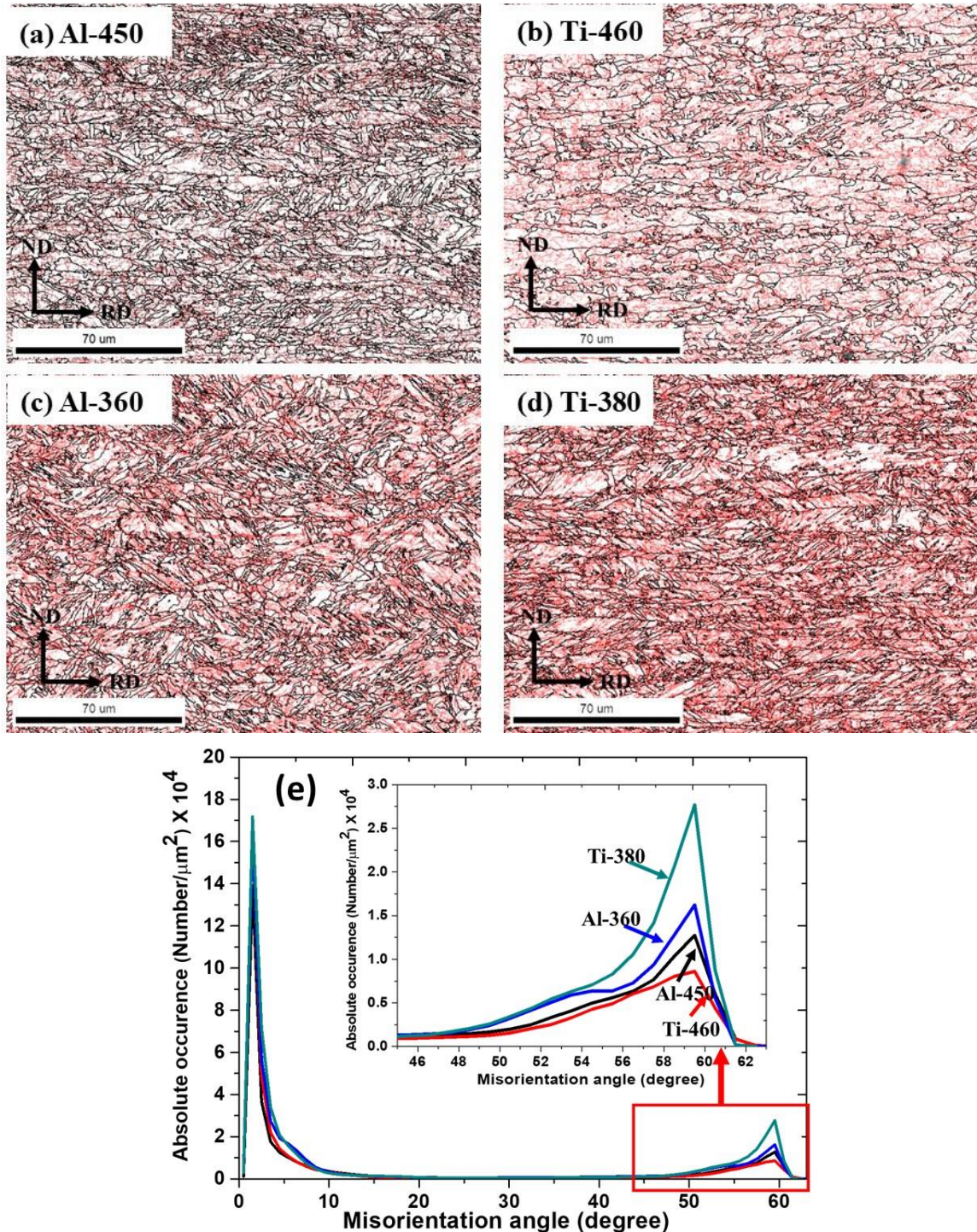


278
 279 **Fig. 7: Kernel average misorientation maps (KAM) considering the first neighbouring
 280 points around the origin, from 0° to 5° misorientation angle as represented by the colour-
 281 code given in each map. The sample codes and the weighted average (wt. avg.) KAM
 282 values are mentioned in the images.**

283 The block- and packet-sizes of TM and LB, preferentially formed during lower
 284 temperature coiling, were also more refined than those of UB and GB, transformed during
 285 higher temperature coiling. Since the block- and packet-boundaries are the HABs, the intensity
 286 of HABs was higher in Ti-380, followed by Al-360. The effective grain sizes (in terms of area
 287 equivalent diameter) were also estimated from the EBSD analysis considering a minimum
 288 misorientation threshold of 15° , i.e., only based on the HABs. Although the prior-austenite
 289 grain structures were elongated along the rolling direction, apart from the prior-austenite grain
 290 boundaries, majority of the martensitic-packet and block-boundaries were also the HABs [46].
 291 As a result, the average aspect ratio values of the ‘effective grains’ in the investigated samples
 292 were not too large (in the range of 1.0 to 2.0) and hence, equivalent circle diameter

representation of effective grain sizes can be justified. The effective grain sizes increased in the following order: Ti-380 ($12.1 \pm 1.0 \mu\text{m}$) < Al-450 ($13.0 \pm 1.5 \mu\text{m}$) < Al-360 ($13.4 \pm 1.3 \mu\text{m}$) < Ti-460 ($14.3 \pm 1.0 \mu\text{m}$).

296



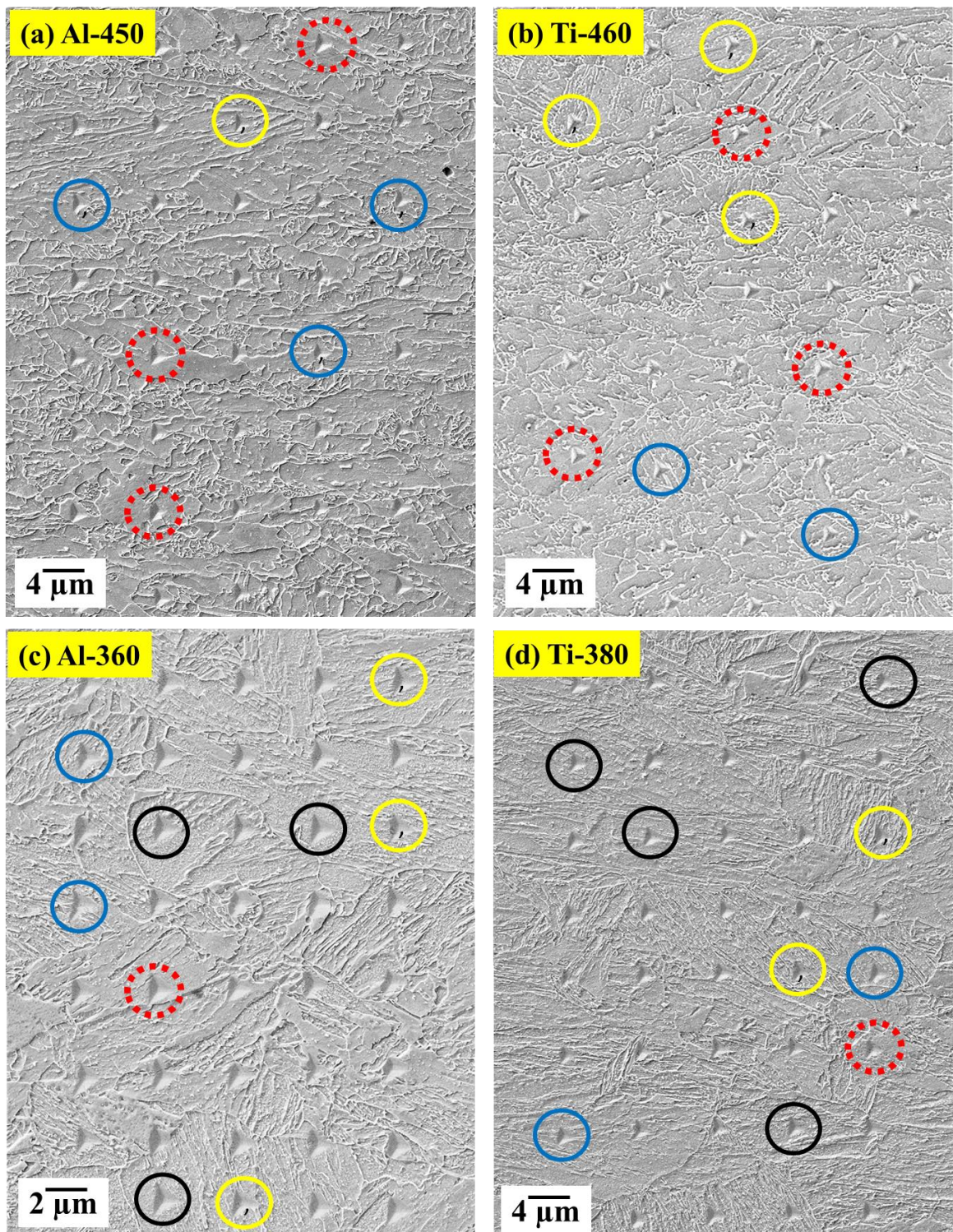
297

298

Fig. 8: (a-d) The EBSD boundary misorientation maps showing the low-angle boundaries, LABs ($2\text{-}15^\circ$ misorientation), and high-angle boundaries, HABs ($>15^\circ$ misorientation), as 'red' and 'black' lines, respectively. (e) The boundary misorientation-angle distribution in terms of absolute frequency of occurrence (number of boundaries per μm^2 area).

303 **3.3. Nanoindentation study on the individual constituents in the strip
304 samples**

305 Instrumented nanoindentation has been carried out to study the individual deformation
306 response of the microstructural constituents under a fixed rate of loading/unloading.
307 Nanohardness was also determined by the method proposed by Oliver and Pharr [69]. **Fig. 9**
308 demonstrates the SEM micrographs of the regions subjected to nanoindentations on different
309 microstructural constituents, which were identified separately and circled in different colors on
310 the respective micrographs. The average nanohardness for each microstructural constituent for
311 a particular sample was derived from at least 100 data and are listed in **Table 3**. **Fig. 10**
312 compares the representative load vs. depth of indentation plots obtained from nanoindentation
313 testing of the individual microstructural constituents in the investigated samples. According to
314 **Fig. 10** and **Table 3**, the nanohardness of the phase constituents followed the general trend,
315 GB < UB < LB < TM. In Al-450, the hardness difference was less between UB and GB, which
316 were considerably softer than LB, **Fig. 10a** and **Table 3**. In Ti-460, the differences in average
317 nano-hardness between GB (soft), UB (intermediate) and LB (hard) were similar, **Fig. 10b** and
318 **Table 3**. In Al-360 and Ti-380, the nanohardness distribution of the phase constituents
319 followed somewhat a dual nature. In Al-360, the hardness differences were less between the
320 two harder constituents (TM and LB) and also between the two softer constituents (GB and
321 UB), **Fig. 10c**. In Ti-380, TM was considerably harder than the other three constituents (LB,
322 UB and GB), which had a similar low hardness response. Overall, the phase constituents in Al-
323 450 had relatively higher average nanohardness (1.3-1.5 times higher) as compared to those in
324 Ti-460. Regarding the samples coiled at lower temperatures, being the predominant
325 constituent, tempered martensite was harder in Ti-380 (1.25 times) as compared to Al-360.

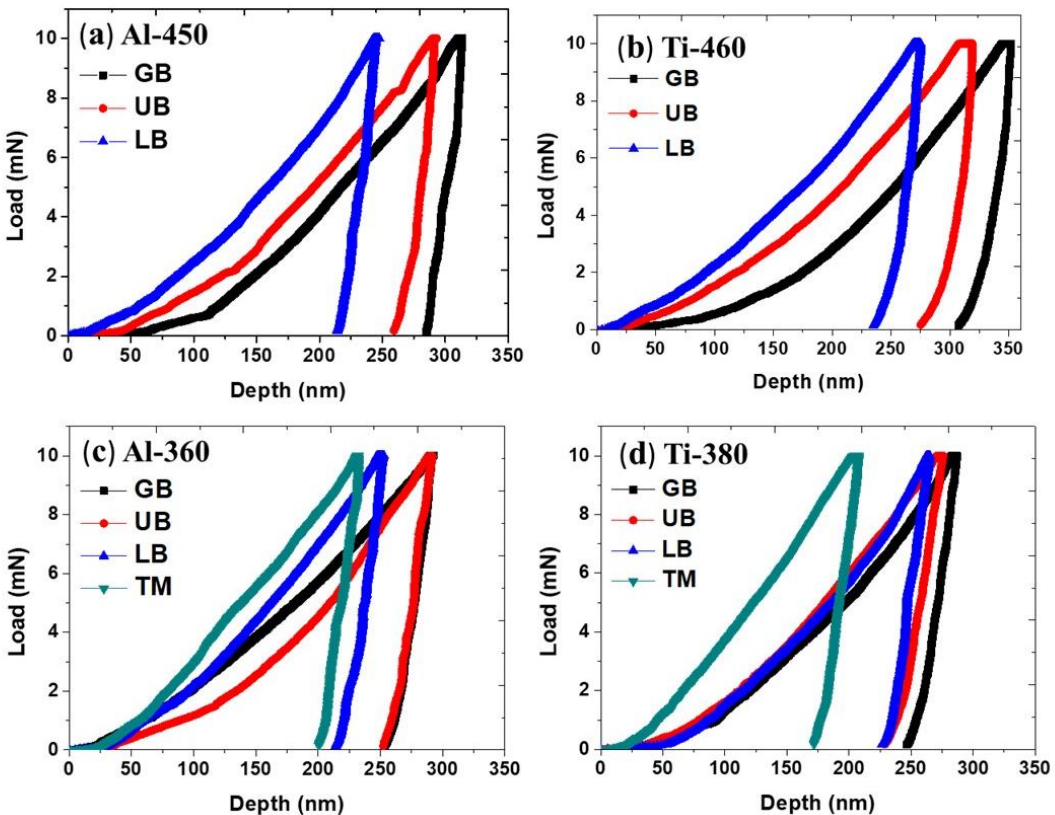


326

327 Fig. 9: SEM micrographs showing with nanoindents from a single grid, on the different
 328 microstructural constituents indicated by different colored circles as follows: GB - Red
 329 dotted; UB - Blue; LB – Yellow; and TM - Black.

330

331



332

333 **Fig. 10:** Representative load vs. depth of indentation plots obtained from nanoindentation
 334 testing for each of the microstructural constituents present in the investigated samples.

335 Table 3: Average nanohardness (in MPa) of the different microstructural constituents.

Microstructural Constituents	Al-450 (MPa)	Al-360 (MPa)	Ti-460 (MPa)	Ti-380 (MPa)
GB	3843 ± 508	4387 ± 794	2528 ± 415	3957 ± 560
UB	4233 ± 544	5028 ± 974	3477 ± 369	5265 ± 808
LB	5797 ± 618	6299 ± 1704	4475 ± 229	6466 ± 789
TM	--	6766 ± 1311	--	8506 ± 929

336

337 The weighted-average nanohardness of a sample (listed in **Table 3**) was calculated
 338 subsequently (based on 400 nanoindentation results) considering the nanohardness values of
 339 all the constituents present in that sample, along with their respective volume fractions (as
 340 reported in **Table 2**). **Fig. 11** shows that average Vickers bulk-hardness and weighted average
 341 nanohardness followed a similar trend. Ti-380 had the maximum hardness, followed by Al-
 342 360, Al-450, and Ti-460. Thus, a decrease in coiling temperature (by 80-90 °C) increased the
 343 hardness, more extensively in the Ti-treated steel. The standard deviation in nanohardness was
 344 higher than the bulk-hardness due to the significantly smaller indent size in nanoindentation
 345 and consequently the stronger effect of local microstructure and its variation.

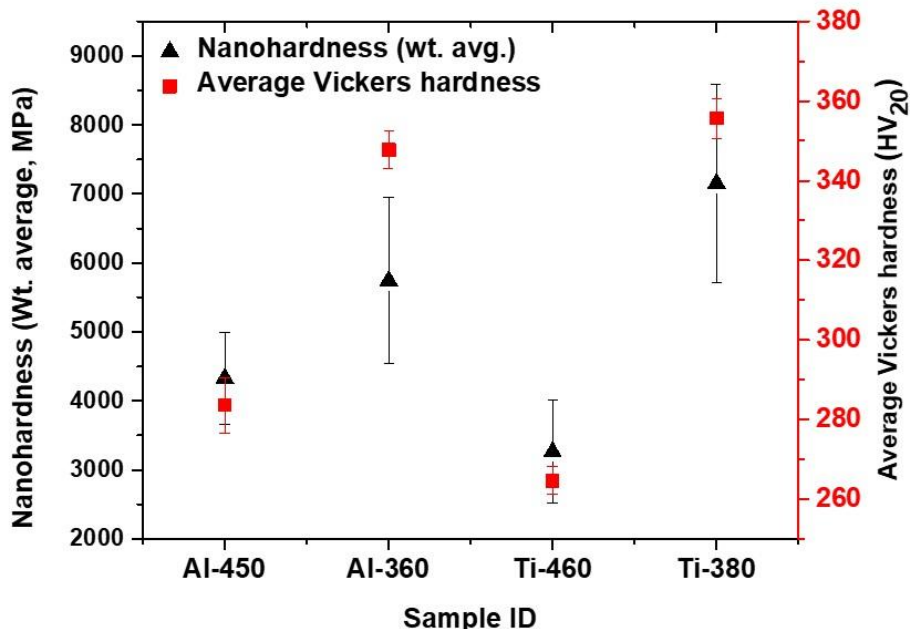


Fig. 11: Weighted average nanohardness along with the average Vickers hardness of the investigated samples.

3.3.1. Determination of strain-hardening exponent ‘n’ by nano-indentation technique

Over the last decade, several studies have been carried out to predict the mechanical properties of the bulk material from the nanoindentation test results [70–75]. Among the available methods, Dao et al. [76] formulated a reverse algorithm-based analysis (called ‘the inverse method’) to estimate the elastic-plastic properties from the load vs. depth of indentation curves as obtained from the nanoindentation experiment. In the present study, the inverse method has been adopted as it is based on a dimensionless function to establish a unique mathematical correlation between the independent quantities that can be obtained from nanoindentation test data. This dimensionless function can be used to estimate the yield strength and strain-hardening exponent (n) from the load vs. depth data in the indentation plot. Further details are available in [76,77]. The strain hardening exponent calculated through instrumented nanoindentation represents the hardening response of each and every microstructural constituent under a small indentation load in a localized region (i.e., at nanometer-scale)

In theory, the plastic behaviour of most metallic materials (pure metal or alloy) can be approximated by a power hardening law, described as [77,78]:

$$\left\{ \begin{array}{ll} \sigma = E\varepsilon & \text{for } \sigma \leq \sigma_{ys} \\ \sigma = \sigma_{ys} \left(1 + \frac{E}{\sigma_y} \varepsilon_p\right)^n & \text{for } \sigma \geq \sigma_{ys} \end{array} \right. \quad (3)$$

where E is the elastic modulus, σ_{ys} is the yield strength, n is the strain hardening exponent and ε_p is the plastic strain which represents the nonlinear part of the total strain (ε) accumulated

370 beyond the yield strain (ε_{ys}), and defined as, $\varepsilon_p = \varepsilon - \varepsilon_{ys}$. Under the sharp Berkovich indenter
 371 having fixed indenter-shape and tip-angle, an elasto-plastic solid normally follows a power law
 372 and the load P can be described as:

$$373 \quad P = P(h, E^*, \sigma_r, n) \quad (4)$$

374 where, h is the indentation depth, E^* is the reduced elastic modulus, and σ_r is the representative
 375 stress corresponding to an arbitrary strain. The present study used $\sigma_{0.033}$ as the representative
 376 stress at $\varepsilon_p = 0.033$ as proposed by Dao et al. [76] to get the following equation:

$$377 \quad \sigma_{0.033} = \sigma_{ys} \left(1 + \frac{E}{\sigma_{ys}} \varepsilon_{0.033} \right)^n \quad (5)$$

378 The representative strain ($\varepsilon_{0.033}$) permits for the construction of a dimensionless function that
 379 is independent of strain-hardening exponent (n) and dependent on the parameter (E^*/ σ_r),
 380 where, E^* is defined as:

$$381 \quad E^* = \left[\frac{1-v^2}{E} + \frac{1-v_i^2}{E_i} \right]^{-1} \quad (6)$$

382 where, E and v are the Elastic modulus and Poisson's ratio of the tested material, respectively,
 383 and subscript 'i' refers to those of the Berkovich indenter ($E_i = 865$ GPa and $v_i = 0.07$). From
 384 the dimensionless analysis, the following function can be generated in which 'CL' is the
 385 proportionality constant defined as load divided by the displacement square, in other words, it
 386 represents the loading curvature of the indentation plot:

$$387 \quad \frac{c_L}{\sigma_{0.033}} = -1.131 \left[\ln \left(\frac{E^*}{\sigma_{0.033}} \right) \right]^3 + 13.635 \left[\ln \left(\frac{E^*}{\sigma_{0.033}} \right) \right]^2 - 30.594 \left[\ln \left(\frac{E^*}{\sigma_{0.033}} \right) \right]^1 + 29.267 \quad (7)$$

388 Once, E, σ_{ys} and $\sigma_{0.033}$ are known, equation (5) can be used to calculate the strain-hardening
 389 exponent (n) of the different microstructural constituents present in the investigated samples,
 390 as listed in **Table 4**.

392
 393 Table 4: Strain hardening exponent (n) of the different microstructural constituents in the
 394 investigated samples.

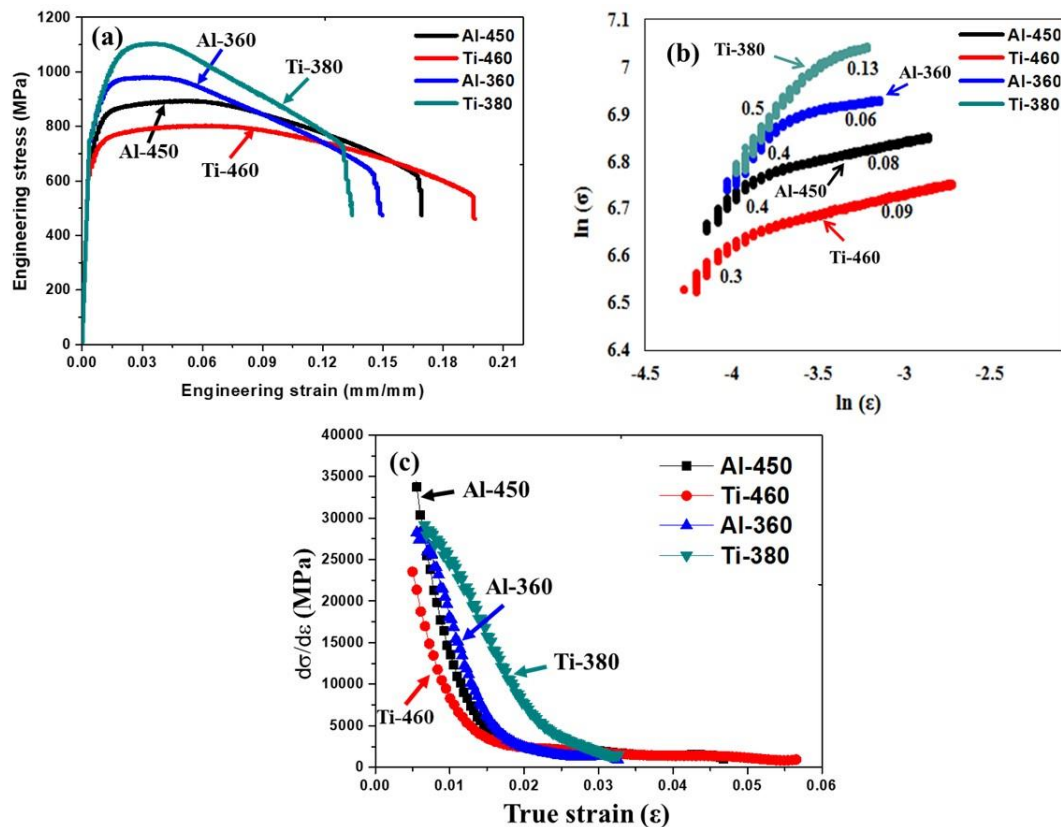
Microstructural Constituents	Al-450	Al-360	Ti-460	Ti-380
GB	0.15 ± 0.01	0.12 ± 0.02	0.12 ± 0.01	0.14 ± 0.01
UB	0.17 ± 0.01	0.31 ± 0.01	0.16 ± 0.01	0.32 ± 0.03
LB	0.22 ± 0.03	0.32 ± 0.01	0.20 ± 0.02	0.33 ± 0.03
TM	-	0.35 ± 0.03	-	0.44 ± 0.04
Wt. avg. of 'n'	0.17	0.33	0.15	0.37

396 **Table 4** indicates that GB and TM had the lowest and highest strain-hardening exponent,
397 respectively. LB had a similar to slightly higher strain-hardening exponent than UB. The ‘n’
398 values of UB and LB were much higher in the samples coiled at lower temperatures than those
399 coiled at higher temperatures. It is interesting to note that the same microstructural constituent
400 shows different hardness and strain-hardening exponent values in different samples. Such a
401 variation can be attributed to the combined effect of differences in steel composition and
402 coiling temperature. The steel composition and coiling temperature decide the driving force for
403 transformation during coiling treatment. At a lower transformation temperature, the higher
404 driving force for transformation and stronger austenite lead to a finer microstructure (i.e.,
405 refined lath size, carbide size etc.). A lower transformation temperature also increases the
406 dislocation density within the transformed constituent. On the other hand, a higher coiling
407 temperature increases any tempering effect on the transformed constituent and the softer the
408 constituent becomes. In addition, a higher coiling temperature increases dynamic recovery of
409 untransformed austenite, which can increase the plate thickness of the transformed product. A
410 refined microstructure and high dislocation density increase the hardness of a constituent. In
411 general, for bainite and martensite, the harder the constituent, the higher is its strain hardening
412 rate [46]. The weighted average ‘n’ value of the sample was also calculated considering the n
413 values of the individual constituents in that sample and their respective volume fractions, and
414 is given in Table 4. A decrease in coiling temperature increased the weighted average ‘n’ values
415 with Ti-380 showing the highest ‘n’ value, followed by Al-360.

416

417 **3.4. Evaluation of tensile properties**

418 Engineering stress-strain curves of the tensile tested specimens are presented in **Fig.**
419 **12. Fig 12a** suggest that both yield strength (σ_{ys}) and ultimate tensile strength (σ_{uts}) increased
420 with the decrease in coiling temperature. Ti-380 showed the maximum strength, with
421 particularly high σ_{uts} , whereas Ti-460 had the minimum strength. An increase in σ_{ys} was
422 accompanied by a decrease in ductility, represented by the percentage of total elongation till
423 fracture. The highest uniform elongation and total elongation were observed in Ti-460 followed
424 by Al-450, whilst, Ti-380 showed the lowest ductility. More details regarding the tensile
425 properties of the investigated samples have discussed in our previous study [11]. The variation
426 in the strain-hardening exponent (n) as the function of true strain is plotted in **Fig. 12b**. The
427 investigated samples showed primarily two stages of work hardening and the hardening
428 exponent (n) at the initial stage increased with the decrease in coiling temperature. Ti-380
429 showed the highest hardening exponents in both the hardening stages. **Fig. 12c** shows the
430 variation in strain-hardening rate ($\frac{d\sigma}{d\varepsilon}$) as the function of true strain. Ti-380 and Ti-460 showed
431 the highest and lowest work hardening rate, respectively, following the trend shown by the ‘n’
432 values at the initial stage of tensile deformation. Al-360 had a slightly higher work-hardening
433 rate than Al-450 despite their similar hardening exponents at the initial stage of deformation.



436 **Fig. 12:** (a) Engineering (tensile) stress-strain plot of the investigated samples; (b) The
 437 change in strain-hardening behaviour with the increase in true stress (σ) and true strain
 438 (ε) based on the Hollomon equation [79]. The 'n' values for different stages of
 439 deformation are mentioned; (c) The variation of strain-hardening rate with the increase
 440 in the true strain of the tested samples. Fig. 12(a, b) are repeated from authors earlier
 441 reference [11].

443 3.5. Assessment of Charpy impact properties

444 The Charpy impact transition curves for the investigated samples are plotted in **Fig. 13**.
 445 The upper shelf energy (USE), the impact energy absorbed at -40°C , and the ductile-to-brittle
 446 transition temperature (DBTT) are listed in **Table 5**.

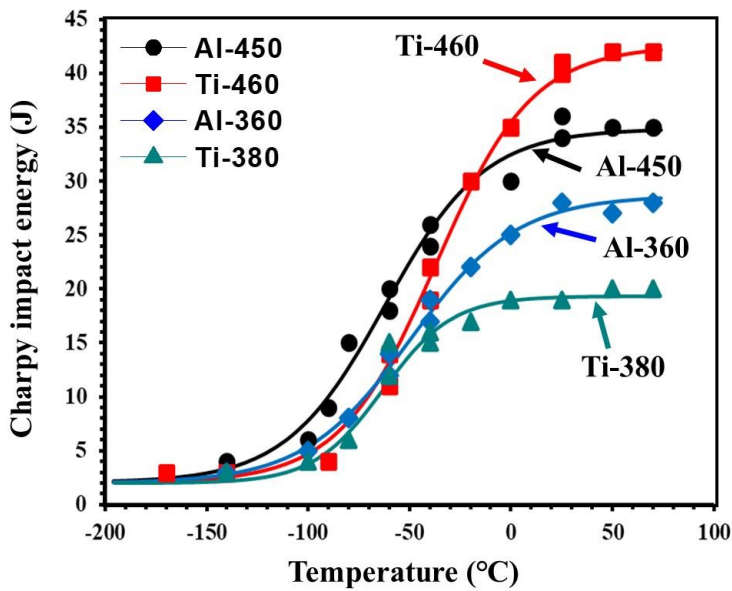


Fig. 13: Charpy impact transition curves of the investigated samples.

447

448

449

450 Table 5: Charpy impact properties of the steel samples.

Sample ID	USE (J)	Impact Energy at -40°C (J)	DBTT (°C)	ITT as per specification (J)	σ_{fd} calculated (MPa)	K_{Jd} Calculated (MPa√m)
Al - 450	35	25	-62	-78	1024	85
Al - 360	29	18	-50	-59	1290	79
Ti - 460	42	20	-37	-61	1001	97
Ti - 380	19	17	-63	-51	1296	45

451 Abbreviations: USE : Upper shelf energy; DBTT : Ductile to the brittle transition temperature;
452 ITT: Impact transition temperature as per specification (27J ITT normalized by specimen cross-
453 section area); σ_{fd} : Dynamic flow stress at 70 °C; K_{Jd} : Dynamic fracture toughness
454

455 According to **Fig. 13** and **Table 5**, Ti-460 showed the highest USE, followed by Al-
456 450, Al-360, and Ti-380. All the investigated samples exhibited brittle fracture with lower shelf
457 energy, LSE, of ~ 2-4 J over the range of -140°C to -170°C. Irrespective of the different USE
458 values, Ti-380 and Al-450 showed similar and low DBTT. The DBTT of Al-360 was lower
459 than that of Ti-460. As per BS EN 10149 specification [2] structural steel grades with yield
460 strength of 700 MPa or higher need to satisfy a minimum Charpy impact toughness of 27J at -
461 40 °C, applicable to a full-size (10 mm × 10 mm) Charpy specimen. Considering the sub-sized
462 (10 mm × 5 mm) test specimens used here (**Fig. 2b**), following a simple energy normalization

procedure, the impact toughness corresponding to the specified 27J impact energy absorption is ~ 13.5 J. The corresponding ITT values (listed in **Table 5** as ‘ITT as per specification’) were lower than -40 °C for all the samples. Al-450 showed the minimum ITT, whilst Ti-380 had the maximum ITT. Ti-460 and Al-360 showed similar and intermediate ITT values. In this context, it is noteworthy that the impact toughness representation in terms of DBTT (temperature corresponding to the impact energy average of USE and LSE) can sometimes be misleading as it primarily depends on the USE, as the LSE lies at a low constant level (say, within 4 J). Considering the significant difference in USE values, initial attention has been paid to understand the difference in USE, and subsequently to explore the variation in ITT.

In the present study, the modified Schindler procedure (MSP) [80,81] was adopted for the prediction of dynamic fracture toughness (K_{Jd}) from the load (P) vs. displacement (δ) curves obtained from the instrumented impact testing at the temperature regime of USE (given in **APPENDIX-1**). According to MSP [80,81], the minimum value of J_{Id} (dynamic elastic-plastic fracture toughness in terms of J-integral) can be estimated from the following equations:

$$J_0 = \frac{7.33.n_d.C_v.10^{-3}}{1-1.47\left(\frac{C_v}{\sigma_{fd}}\right)} \quad (8)$$

$$J_{0.2} = 3.92. n_d^{\frac{1}{3}}. C_v. 10^{-3} \quad (9)$$

$$J_{0.2t} = 11.44. n_d^{\frac{1}{3}}. C_v \left\{ \left(\frac{3.05 C_v}{10^3 \sigma_{fd}} \right)^3 \cdot n_d^{\frac{1}{3}} + 0.2 \right\}^{2/3} \cdot 10^{-3} \quad (10)$$

where, J_0 is for crack extension, $\Delta a = 0$ mm; $J_{0.2}$ is for $\Delta a = 0.2$ mm, and $J_{0.2t}$ is for $\Delta a = 0.2$ mm from the intersection of the blunting-line with the J–R curve [81]; C_v is the Charpy impact energy; and n_d is dynamic strain hardening exponent. σ_{fd} is dynamic flow stress which can be further estimated from the following equation [82]:

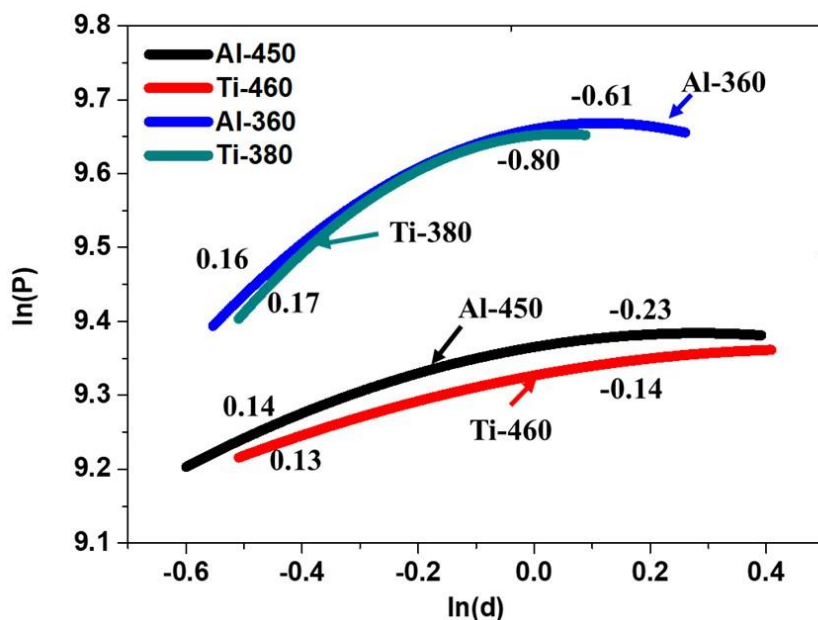
$$\sigma_{fd} = \frac{2.99.P_{fd}.W}{B.(W-a_0)^2} \quad (11)$$

where, P_{fd} is the average of general yield load and maximum load as obtained from the load-displacement plot recorded by the instrumented impact test system for the specimens tested at 70°C (**APPENDIX-1**). B (6 mm / 8 mm) is the thickness, W (10 mm) is the width and a_0 (2 mm) is the machined notch-depth of the Charpy impact test specimen. Furthermore, the dynamic strain hardening exponent (n_d) was estimated from the instrumented impact tests by fitting the following power-law relationship [83] within the data points falling between the general yield load (P_{gy}) and the maximum load (P_{max}) of the load (P) - displacement (δ) plot:

$$P = A. \delta_{pl}^{n_d} \quad (12)$$

Where, P, A, δ_{pl} , and n_d are the load, fitting parameter, plastic displacement, and dynamic strain hardening exponent, respectively. Dynamic work-hardening characteristics of the investigated steels during Charpy impact testing is plotted in **Fig. 14**. Similar to the static strain-hardening (**Fig. 12b**), the dynamic strain-hardening appeared to generally follow a two-stage behaviour,

497 **Fig. 14.** The n_d values for the first- and second-stage of dynamic strain-hardening are given in
 498 **Fig 14.** The positive and negative n_d values during the first- and second-stage of strain-
 499 hardening, respectively, indicate that although strain-hardening governed initially, dynamic
 500 softening mechanism gradually dominated over the strain-hardening during the latter part of
 501 deformation. Such a negative hardening exponent can arise from adiabatic heating of the
 502 material under high strain-rate loading that locally increases the temperature, leading to
 503 dynamic recovery induced softening [84]. Hence, the positive n_d values associated with the
 504 first stage of deformation (less influenced by temperature) were used to calculate the dynamic
 505 elastic-plastic fracture toughness.



506
 507 **Fig. 14: Dynamic strain-hardening behaviours of the investigated steel samples showing
 508 different hardening exponents. (Calculations were done based on equation 12).**
 509

510 According to Schindler et al. [81], J_0 provides a more conservative estimation of J_{Id} . Hence,
 511 the dynamic fracture toughness in terms of dynamic stress-intensity factor, K_{Jd} was calculated
 512 from J_0 (equation 8) using the following equation [79–85]:

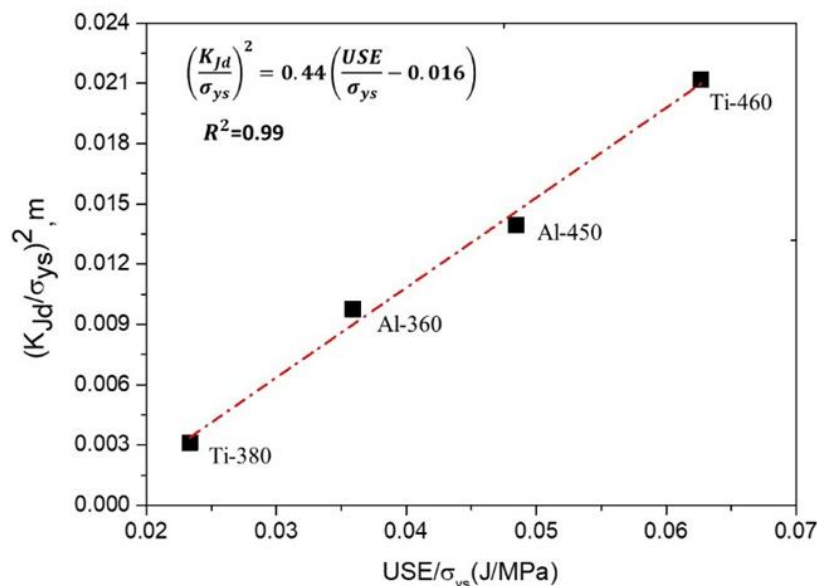
513
$$K_{Jd} = \sqrt{E * J_{Id}} \quad (13)$$

514 where E is Young's modulus of the steel and $J_{Id}=J_0$. The calculated σ_{fd} and K_{Jd} values are listed
 515 in **Table 5**. The K_{Jd} values follow the same trend as the USE values obtained from Charpy
 516 impact testing. The calculated σ_{fd} values, on the other hand, obeys the trend shown by the
 517 strength of the samples in quasi-static tensile testing.

518 Barsom and Rolfe [79,86] proposed the following correlation between the dynamic
 519 fracture toughness under mode-I (K_{Id}) and the upper shelf energy (USE) for the high-strength
 520 (σ_{ys} 760 - 1700 MPa) metallic alloys:

521
$$\left(\frac{K_{Id}}{\sigma_{ys}}\right)^2 = A \left(\frac{USE}{\sigma_{ys}} - B\right) \quad (14)$$

522 where A and B are proportionality constants. It is to be noted that such correlations depend on
 523 factors such as the material tested, test temperature range, loading rate, and notch-design and
 524 accuracy. However, at the USE regime, the effects of temperature, loading rate and notch-
 525 acuity are not as severe as in the impact transition temperature regime [79]. To derive a
 526 relationship between K_{Id} (K_{Jd} used as K_{Id} in equation 14) and USE, those are plotted in **Fig.**
 527 **15** (with correlation coefficient, $R^2 = 0.99$). Regression analysis has been employed to find out
 528 the values of different constants for the given relationship. The proposed equation (in the same
 529 form as suggested by Barsom and Rolfe [79], and Tanaka et al. [87]) is mentioned in **Fig. 15**.
 530 In future, the applicability of this relationship needs to be verified for other UHSS systems.



531
 532 **Fig. 15: Relation between calculated K_{Jd} and upper shelf energy (USE) values of the**
 533 **impacted tested samples of the investigated steels.**

535 **3.6. Fractography study on the impact tested specimens**

536 The SEM fractographs of the broken Charpy specimens impact tested at the USE
 537 regime (+70°C) are given in **Fig. 16**. Al-450 and Ti-460 showed a completely ductile ‘fibrous-
 538 fracture appearance’ characterized by the presence of numerous dimples on the fracture
 539 surfaces. Some of the large dimples were elongated along the longitudinal direction (i.e., RD
 540 of the originally rolled strips), following the elongated grain structures in **Fig. 3**. Those voids
 541 possibly initiated around the carbide particles situated at the prior austenite grain boundaries,

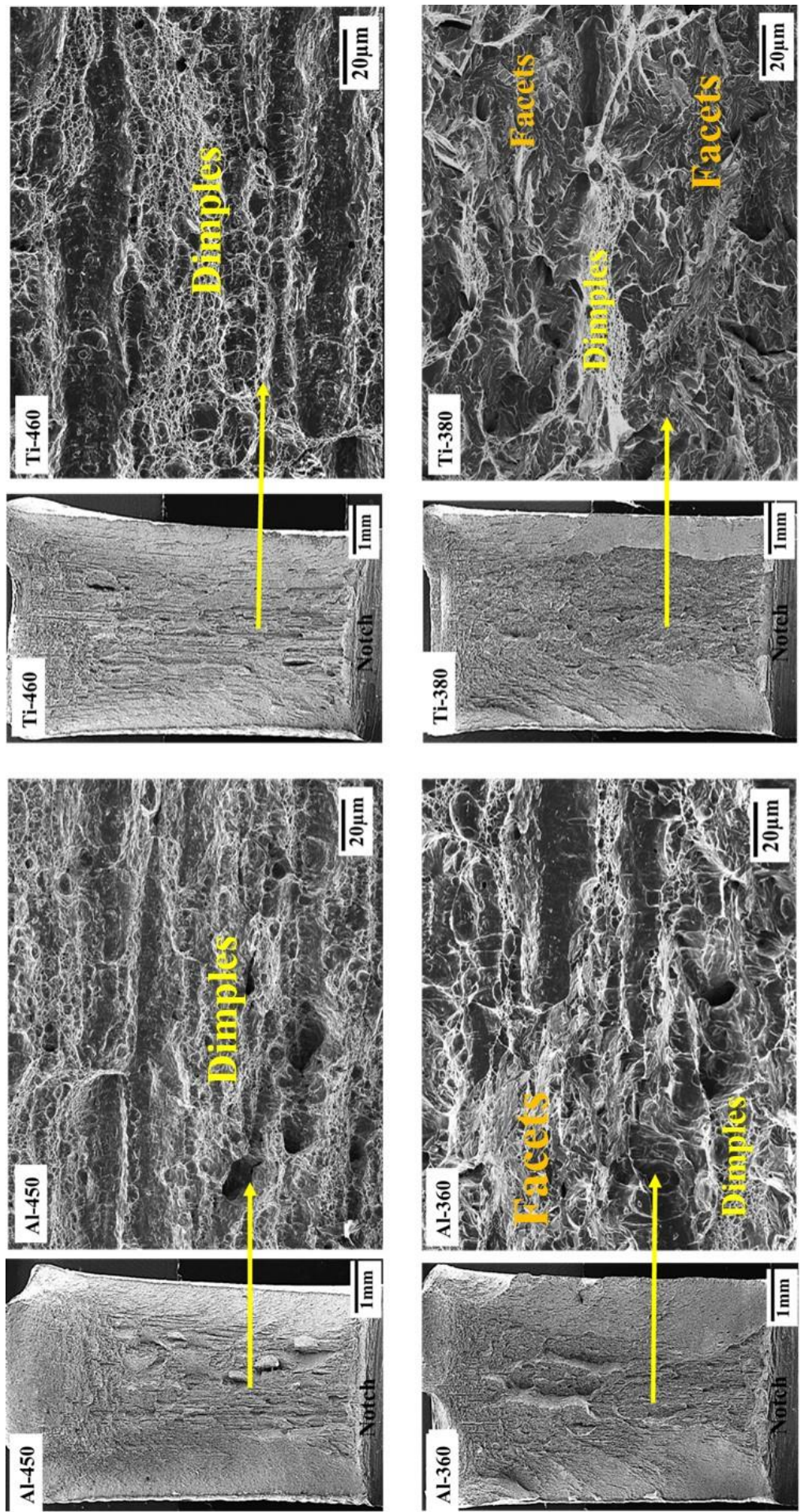
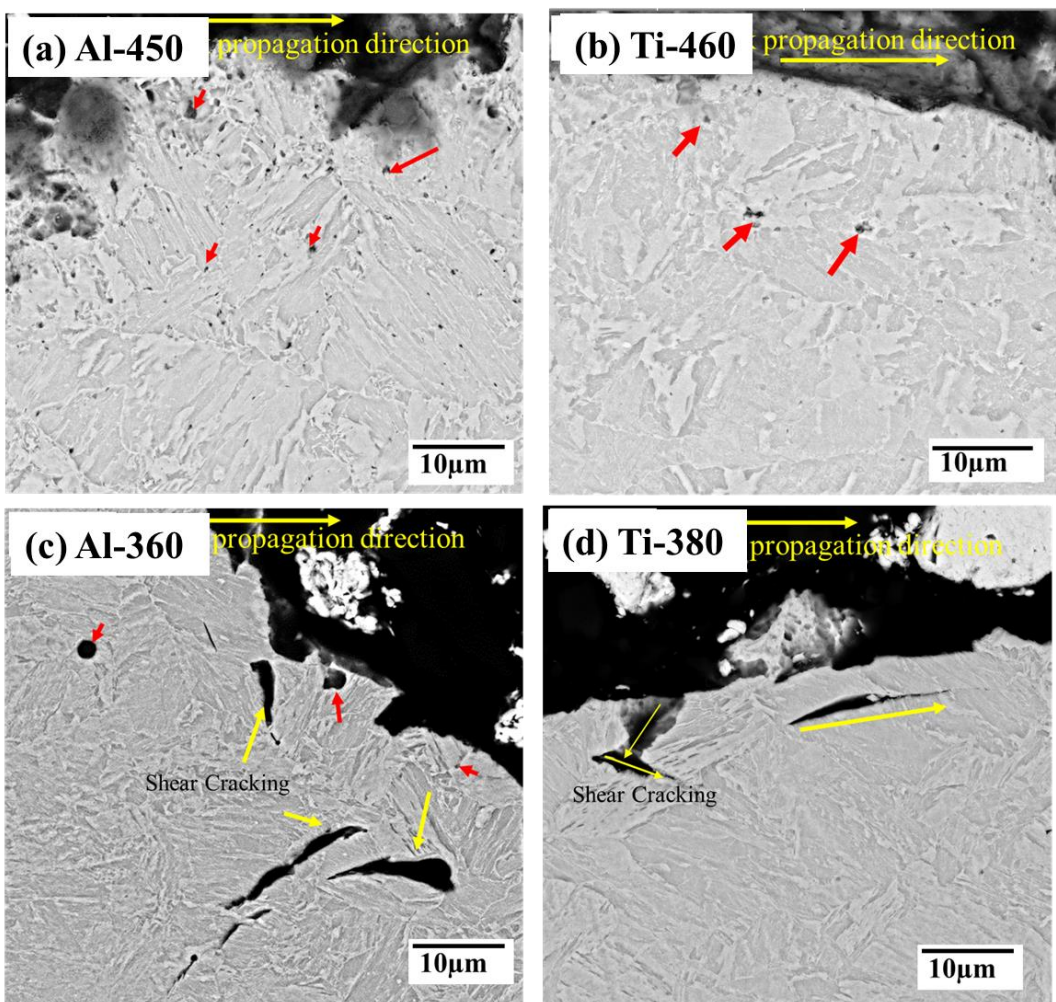


Fig. 16: Low magnification fractographs of Charpy impact tested samples broken at +70 °C along with high magnification images to understand the mode of fracture.

543 or the interphase boundaries between the different phase constituents, and grew along those
 544 boundaries, resulting in an elongated appearance. It is noteworthy that even at USE regime,
 545 besides fibrous fracture, quasi-cleavage fracture covered around 25 percent of the fracture
 546 surface in Al-360, and prominent cleavage facets dominated the fracture surface (covering 80
 547 percent area) in Ti-380.

548 The SEM micrographs showing the locations just beneath the fracture surfaces on the
 549 transverse cross-sections of the broken Charpy specimens are shown in **Fig. 17**. Several fine
 550 voids were uniformly distributed below the fracture surface in Al-450 up to a depth of ~ 80
 551 µm, **Fig. 17a**. The void density was less in Ti-460, and the voids were primarily located just
 552 below the fracture surface within a depth of ~ 20 µm, **Fig. 17b**. The size and density of the
 553 voids decreased with the increase in the distance below the fracture surface, **Fig. 17(a, b)**. In
 554 Al-360 and Ti-380, apart from a few large voids, there were several secondary cracks, either
 555 formed along with the shear bands (shear cracking) or the unpropagated cleavage cracks, **Fig.**
 556 **17(c, d)**.



557
 558 **Fig. 17:** The SEM micrographs of the location just below the fracture surface (on the
 559 transverse section plane, perpendicular to the fracture surface) showing the voids (red
 560 arrows) and cracks (yellow arrows).

561 **4. Discussion on the microstructure – strength – impact toughness**
562 **correlation**

563 The microstructural evolution in the rolled and coiled strips, considering the steel
564 compositions and processing parameters, has been discussed in our earlier study [11]. The
565 emphasis of this study is to investigate the microstructure-tensile-impact toughness
566 relationship. The higher ductility and USE of Ti-460 followed by Al-450 can be attributed to
567 the presence of softer constituents (GB and UB) at a high fraction having low dislocation
568 densities, **Table 2** and **Section 3.2**. Voids nucleate primarily around the carbide particles and
569 MA constituents. According to the Rice and Tracey model [88], void growth is promoted at a
570 lower yield strength, lower strain hardening rate and higher plastic strain accommodation in
571 the ductile matrix. The greater the amount of void growth, the higher the energy absorption for
572 plastic deformation, and the higher the ductility and USE [79,88].

573 The differences in local deformation response between the microstructural constituents
574 (namely, GB, UB and LB) were small, with the properties being in a similar range in Ti-460,
575 **Fig. 10b** and **Table 3**. In contrast, LB was considerably harder than UB and GB in Al-450,
576 **Fig. 10a** and **Table 3**. As a result, the development of plastic deformation was more gradual
577 and uniform in Ti-460 as compared to Al-450. In our earlier paper [11], the microstructural
578 heterogeneity in the investigated steels has been quantified based on the hardness variation and
579 represented by a heterogeneity index. Ti-460 showed superior microstructural homogeneity
580 than that in Al-450. More uniform deformation of the softer matrix in Ti-460 possibly reduced
581 the extent of void nucleation and promoted void growth, contributing to its higher ductility and
582 USE.

583 Contrary to Ti-460 and Al-450, the higher strength and lower USE of Ti-380 and Al-
584 360 can be attributed to the high fraction of harder constituents (TM and GB) with high
585 dislocation densities, **Table 2** and **Section 3.2**. The TM in Ti-380 was harder than that of Al-
586 360, **Table 3**, and it can be explained as follows. Bainitic transformation is accompanied by
587 rejection of C from bainite that enriches the C content in the adjacent austenite [46]. A higher
588 fraction of bainite in Ti-380 resulted in higher C content in the austenite and subsequently in
589 the transformed martensite, as compared to that in Al-360. Besides, during bainite formation,
590 the transformation strain is accommodated by the generation of dislocations in the adjacent
591 austenite. Those dislocations are inherited by martensite after austenite to martensite
592 transformation [46]. Due to the higher bainite fraction, the dislocation density was also higher
593 in the martensite in Ti-380. Overall, higher hardness and strength strongly restricted the plastic
594 deformation in Ti-380, followed by Al-360. Hence, cleavage and quasi-cleavage fracture
595 occurred even at the higher test temperatures, **Fig. 16**, reducing the USE. Besides, the high
596 hardness difference between the harder and softer constituents resulted in preferential
597 deformation of softer constituents (present at a lower fraction), under a high constraint from
598 harder constituents. Such a severe deformation heterogeneity can result in (i) shear banding

599 and the associated shear cracking within the softer constituents, and (ii) cleavage cracking
600 within the harder constituents, **Fig. 17(c, d)**. The high strength and considerable post-uniform
601 elongation (9.6-11.4 %) seen for Ti-380 and Al-350 could be due to their high strain-hardening
602 ability, which resisted void coalescence [89]. Relating tensile toughness (area under the tensile
603 curve, in MJ/m^3) and USE (in J), Ti-380 and Al-360 had similar tensile toughness (~ 131
604 MJ/m^3) despite different USE (19 J and 29 J, respectively), while, for Al-450 (139 MJ/m^3 , 35
605 J) and Ti-460 (145 MJ/m^3 , 42 J) these parameters follow a similar trend.

606 It is interesting to note that the weighted average strain hardening exponent calculated
607 from instrumented nanoindentation (Table 4) and the strain hardening exponent (n) obtained
608 from the tensile test (Fig. 12b) showed some difference. The weighted average strain-hardening
609 exponents (n) estimated from nanoindentation testing (in Table 4) are significantly different
610 for the samples coiled at higher temperatures (0.15-0.17) and lower temperatures (0.33-0.37).
611 However, the ‘n’ values obtained from tensile testing (Fig. 12b) are within a close range (0.3-
612 0.5) even at the initial stage of deformation. The difference between the average strain-
613 hardening exponents estimated from nanoindentation testing and obtained from tensile testing
614 is more prominent in the samples of Al-treated steels. According to the nano-indentation test,
615 the strain hardening component of Al-360 is two times higher than that of Al-450 (Table 4).
616 However, according to the tensile test results in Fig. 12(b), both materials have similar strain
617 hardening exponent value (i.e., $n \sim 0.4$). The samples coiled at lower temperatures contain
618 much higher amounts of lower bainite and tempered martensite (78-82 %) which show high
619 ‘n’ values at a local scale (0.32-0.44, Table 4). During tensile deformation of those samples,
620 possibly those constituents governed the strain-hardening rate even at the initial stage of
621 deformation. In contrast, the microstructure of the samples coiled at higher temperatures are
622 dominated by upper bainite and granular bainite (75-90 %) having lower ‘n-values’ at the local
623 scale (0.12-0.17). The UB and GB in the higher temperature coiled samples are also relatively
624 softer (nanohardness values 2528-4233 MPa) than the same constituents in the lower
625 temperature coiled samples (3957-5265 MPa), Table 3. Therefore, it appears that during tensile
626 deformation, GB and UB in the higher temperature coiled samples strain-hardened rapidly
627 resulting in the high overall strain-hardening exponent, as compared to that of the individual
628 constituents. The weighted average n-values calculated and listed in Table 4 are based on the
629 assumption that all the individual constituents deform simultaneously. That may not be true in
630 tensile testing where there can be a strain-partitioning effect during the deformation of bulk
631 material resulting in preferential deformation of softer constituents [90], their rapid strain-
632 hardening, and subsequently the deformation of all the constituents. Besides, as and when
633 softer constituents deform in the presence of harder constituents, geometrically necessary
634 dislocations are generated within the deforming constituents due to constraint from the harder
635 entities. As a result, softer constituents can strain-harden rapidly. In contrast, during
636 nanoindentation testing each and every constituent deformed almost individually without

637 significant effect of the neighbouring entities and dislocations generated are only due to the
638 indentation.

639 A difference in strain-hardening behavior between tensile and nanoindentation testing
640 could also be due to the difference in the state of stress and strain distribution. First of all, in
641 tensile testing, the bulk material deforms under a uniaxial state of stress over the uniform
642 deformation regime. In nanoindentation, the stress state underneath the indenter is a
643 local and triaxial stress. Besides, the stress distribution in the depth-sensing
644 nanoindentation technique is much more complex than in the uniaxial tensile test [91,92].
645 In case of the Berkovich pyramid indenter, friction at the indenter-metal interface also
646 influences the plastic flow [77]. It has been found that the prediction of tensile properties
647 from the instrumented nanoindentation technique also requires correction factors
648 considering plastic pile-up / sink-in phenomenon and elastic deflection of the material
649 [93,94]. All these aspects deserve more attention in future studies.

650 Apart from the influence of USE levels, as mentioned earlier, ITT can depend on the
651 resistance offered by the matrix to cleavage crack propagation over the impact transition
652 regime. The lowest ITT (and also low DBTT) of Al-450 sample can be attributed to its low
653 effective grain size (restricting cleavage crack propagation) along with a deformable matrix. In
654 spite of the lowest USE, the ITT of Ti-380 is not too high either, possibly due to its low
655 effective grain size and high intensity of HABs. Overall, ITT depends on the following two
656 factors: (i) Low effective grain size and high intensity of HABs that effectively retarded the
657 cleavage crack propagation (LABs are ineffective in that respect [95]); (ii) As the crack
658 initiated in hard constituents, entered the softer constituents crossing the interphase boundaries
659 the dislocation emission at the crack-tip possibly shielded the crack-tip and reduced the crack
660 velocity [96,97].

661 The present study demonstrates that coiling temperature has a significant influence on
662 the microstructure and properties of the investigated UHSS strips. In the samples coiled at
663 higher temperatures (450-460 °C), the microstructure comprising different forms of bainite
664 ensures superior ductility and impact properties with a relatively lower strength. On the other
665 hand, in the samples coiled at lower temperatures (360-380 °C), the microstructure, dominated
666 by tempered martensite and lower bainite, offers higher strength, but inferior ductility and
667 impact toughness. It may be possible to achieve a better combination of strength and toughness
668 at an intermediate coiling temperature (say, 400-420 °C) which needs to be explored in future.
669 The microstructure and properties of Al-treated and Ti-treated steel samples are very similar,
670 for a particular coiling temperature range. Therefore, either of these treatments can be adopted
671 to protect B in these steels. In an earlier investigation [11], Ti-460 showed the best room
672 temperature bending performance, followed by Al-360. Overall, considering the high ductility,
673 bendability and impact properties, future research may be focused on increasing the strength
674 of Ti-460 sample (at least to achieve a yield strength more than 700 MPa).

675 **5. Conclusions:**

676

677 The tensile and Charpy impact properties of four strip samples from two different B-
678 added low-C ultra-high-strength steel strips (Al-treated and Ti-treated), coiled at two different
679 temperature ranges (360-380°C and 450-460°C), have been evaluated and correlated to the
680 microstructural parameters. The major conclusions derived from the study are listed below:

- 681 • Regarding Ti-460 and Al-450 samples coiled at higher temperatures, the presence of a
682 high-fraction (75-90%) of softer constituents, i.e., upper bainite (UB) and granular
683 bainite (GB) with low dislocation densities decreased the strength (yield strength 670-
684 722 MPa), however, improved the ductility (16.9-19.5 %) and upper shelf energy (USE
685 35-42 J).
- 686 • In contrast, for Al-360 and Ti-380 samples coiled at lower temperatures, a high fraction
687 (78-82%) of harder constituents, i.e., tempered martensite (TM) and lower bainite (LB)
688 increased the strength (yield strength 808-814 MPa), however, reduced the ductility
689 (13.0-14.5 %) and upper shelf energy (USE 19-29 J).
- 690 • In general, the hardness and strain-hardening ability were higher in the case of Al-360
691 and Ti-380 samples containing a higher fraction of TM and LB as compared to the rest.
692 In this regard, the same trend was obtained from nanoindentation testing, bulk-hardness
693 testing, quasi-static tensile testing and dynamic Charpy impact testing. Such a trend has
694 rarely been reported in the literature.
- 695 • At the USE regime, the fracture surfaces of Ti-460 and Al-450 showed predominantly
696 ductile ‘fibrous-fracture appearance’, whilst, the fracture surfaces of Al-360 and Ti-380
697 showed quasi-cleavage and cleavage fracture appearance, apart from fibrous fracture.
- 698 • Despite the low USE, Ti-380 showed the lowest DBTT (-63°C), followed by Al-450 (-
699 62°C) due to the high intensity of high-angle boundaries, and especially the low
700 effective grain size. The USE levels could also have influenced the DBTT values.
- 701 • The following empirical equation has been proposed to relate the dynamic mode-I
702 fracture toughness (K_{Id}) and the USE for the investigated UHSS:

$$703 \quad \left(\frac{K_{Id}}{\sigma_{ys}} \right)^2 = 0.44 \left(\frac{USE}{\sigma_{ys}} - 0.016 \right)$$

704

705 **Acknowledgement:**

706 Authors gratefully acknowledge Department of MME and CRF, IIT Kharagpur for the
707 experimental facilities, and WMG-University of Warwick for providing the materials.

708

709 **APPENDIX-I**

711 Fig. A1: Load vs. displacement curves obtained from instrumented Charpy impact testing of
712 the specimens at +70°C. The crack propagation energy calculated from the load-displacement
713 curves are mentioned in the images.

714

715 **References:**

- 716 [1] S. Matsuoka, K. Hasegawa, Y. Tanaka, Newly-Developed Ultra-High Tensile Strength
717 Steels with Excellent Formability and Weldability, 10 (2007) 13–18.
- 718 [2] (CEN) European Committee for Standardisation, BS EN 10149-1:2013 Hot rolled flat
719 products made of high yield strength steels for cold forming Part 1 : General technical
720 delivery conditions, (2013).
721 <https://shop.bsigroup.com/ProductDetail?pid=000000000030239495> (accessed April
722 24, 2021).
- 723 [3] ASTM A673 / A673M - 17 Standard Specification for Sampling Procedure for Impact
724 Testing of Structural Steel, (n.d.). <https://www.astm.org/Standards/A673.htm> (accessed
725 April 24, 2021).
- 726 [4] D. Liu, B. Cheng, M. Luo, F460 Heavy Steel Plates for Offshore Structure and
727 Shipbuilding Produced by Thermomechanical Control Process, ISIJ Int. 51 (2011) 603–
728 611. <https://doi.org/10.2355/isijinternational.51.603>.
- 729 [5] W. Schütz, F. Schröter, Development of heavy steel plate for mayflower resolution,
730 special purpose vessel for erection of offshore wind towers, Mater. Sci. Technol. 21
731 (2005) 590–596. <https://doi.org/10.1179/174328405X38339>.
- 732 [6] Z. Shang, J. Ding, C. Fan, M. Song, J. Li, Q. Li, S. Xue, K.T. Hartwig, X. Zhang,
733 Tailoring the strength and ductility of T91 steel by partial tempering treatment, Acta
734 Mater. 169 (2019) 209–224. <https://doi.org/10.1016/j.actamat.2019.02.043>.
- 735 [7] J. Xue, Z. Zhao, C. Bin, X. Liu, H. Wu, H. Li, W. Xiong, Effects of rolling and coiling
736 temperature on the microstructure and mechanical properties of hot-rolled high strength
737 complex phase steel, Mater. Res. Express. 6 (2019) 0965c8.
738 <https://doi.org/10.1088/2053-1591/ab1404>.
- 739 [8] S.J. Kim, C.G. Lee, T.H. Lee, S. Lee, Effects of coiling temperature on microstructure
740 and mechanical properties of high-strength hot-rolled steel plates containing Cu, Cr and
741 Ni, ISIJ Int. 40 (2000) 692–698. <https://doi.org/10.2355/isijinternational.40.692>.
- 742 [9] L. Xu, H. Wu, Q. Tang, Effects of coiling temperature on microstructure and
743 precipitation behavior in Nb–Ti microalloyed steels, ISIJ Int. 58 (2018) 1086–1093.
744 <https://doi.org/10.2355/isijinternational.ISIJINT-2017-614>.
- 745 [10] M. Sun, Y. Xu, W. Du, Influence of coiling temperature on microstructure, precipitation
746 behaviors and mechanical properties of a low carbon Ti micro-alloyed steel, Metals
747 (Basel). 10 (2020) 1–10. <https://doi.org/10.3390/met10091173>.
- 748 [11] A. Mandal, A. Karmakar, D. Chakrabarti, C. Davis, Effect of Alloying and Coiling
749 Temperature on the Microstructure and Bending Performance of Ultra-High-Strength
750 Strip Steel, Metall. Mater. Trans. A Phys. Metall. Mater. Sci. 49 (2018) 6359–6374.
751 <https://doi.org/10.1007/s11661-018-4946-z>.
- 752 [12] R.O. Ritchie, The conflicts between strength and toughness, Nat. Mater. 10 (2011) 817–
753 822. <https://doi.org/10.1038/nmat3115>.
- 754 [13] F.G. Caballero, J. Chao, J. Cornide, C. García-Mateo, M.J. Santofimia, C. Capdevila,
755 Toughness deterioration in advanced high strength bainitic steels, Mater. Sci. Eng. A.
756 525 (2009) 87–95. <https://doi.org/10.1016/j.msea.2009.06.034>.
- 757 [14] J. Kobayashi, D. Ina, A. Futamura, K. Sugimoto, Fracture Toughness of an Advanced
758 Ultrahigh-strength TRIP-aided Steel, ISIJ Int. 54 (2014) 955–962.

- 759 https://doi.org/10.2355/isijinternational.54.955.
- 760 [15] H. Nathani, D.K. Misra, J. Hartmann, S.G. Jansto, Some Physical Metallurgy Aspects
761 of High Strength Hot Rolled Nb-Ti Microalloyed Steels with Superior Fracture
762 Resistance and Formability, *Mater. Sci. Technol.* 3 (2004) 1–5.
- 763 [16] A.K. Lis, Mechanical properties and microstructure of ULCB steels affected by
764 thermomechanical rolling, quenching and tempering, *J. Mater. Process. Technol.* 106
765 (2000) 212–218. [https://doi.org/10.1016/S0924-0136\(00\)00616-6](https://doi.org/10.1016/S0924-0136(00)00616-6).
- 766 [17] Y. Shao, C. Liu, Z. Yan, H. Li, Y. Liu, Formation mechanism and control methods of
767 acicular ferrite in HSLA steels: A review, *J. Mater. Sci. Technol.* 34 (2018) 737–744.
768 <https://doi.org/10.1016/j.jmst.2017.11.020>.
- 769 [18] J.B. Seol, D. Raabe, P.P. Choi, Y.R. Im, C.G. Park, Atomic scale effects of alloying,
770 partitioning, solute drag and austempering on the mechanical properties of high-carbon
771 bainitic-austenitic TRIP steels, *Acta Mater.* 60 (2012) 6183–6199.
772 <https://doi.org/10.1016/j.actamat.2012.07.064>.
- 773 [19] K.I. Sugimoto, Fracture strength and toughness of ultra high strength TRIP aided steels,
774 *Mater. Sci. Technol.* 25 (2009) 1108–1117.
775 <https://doi.org/10.1179/174328409X453307>.
- 776 [20] T. Inoue, F. Yin, Y. Kimura, K. Tsuzaki, S. Ochiai, Delamination effect on impact
777 properties of ultrafine-grained low-carbon steel processed by warm caliber rolling,
778 *Metall. Mater. Trans. A Phys. Metall. Mater. Sci.* 41 (2010) 341–355.
779 <https://doi.org/10.1007/s11661-009-0093-x>.
- 780 [21] A. Zare, A. Ekrami, Influence of martensite volume fraction on impact properties of
781 triple phase (TP) steels, *J. Mater. Eng. Perform.* 22 (2013) 823–829.
782 <https://doi.org/10.1007/s11665-012-0312-2>.
- 783 [22] I. De Diego-Calderón, M.J. Santofimia, J.M. Molina-Aldareguia, M.A. Monclús, I.
784 Sabirov, Deformation behavior of a high strength multiphase steel at macro- and micro-
785 scales, *Mater. Sci. Eng. A* 611 (2014) 201–211.
786 <https://doi.org/10.1016/j.msea.2014.05.068>.
- 787 [23] Y. Chang, M. Lin, U. Hangen, S. Richter, C. Haase, W. Bleck, Revealing the relation
788 between microstructural heterogeneities and local mechanical properties of complex-
789 phase steel by correlative electron microscopy and nanoindentation characterization,
790 *Mater. Des.* 203 (2021) 109620. <https://doi.org/10.1016/j.matdes.2021.109620>.
- 791 [24] E.A. Ariza-Echeverri, M. Masoumi, A.S. Nishikawa, D.H. Mesa, A.E. Marquez-Rossy,
792 A.P. Tschiptschin, Development of a new generation of quench and partitioning steels:
793 Influence of processing parameters on texture, nanoindentation, and mechanical
794 properties, *Mater. Des.* 186 (2020) 108329.
795 <https://doi.org/10.1016/j.matdes.2019.108329>.
- 796 [25] N. Fujita, N. Ishikawa, F. Roters, C.C. Tasan, D. Raabe, Experimental-numerical study
797 on strain and stress partitioning in bainitic steels with martensite-austenite constituents,
798 *Int. J. Plast.* 104 (2018) 39–53. <https://doi.org/10.1016/j.ijplas.2018.01.012>.
- 799 [26] I. de Diego-Calderón, D. De Knijf, M.A. Monclús, J.M. Molina-Aldareguia, I. Sabirov,
800 C. Föjer, R.H. Petrov, Global and local deformation behavior and mechanical properties
801 of individual phases in a quenched and partitioned steel, *Mater. Sci. Eng. A* 630 (2015)
802 27–35. <https://doi.org/10.1016/j.msea.2015.01.077>.
- 803 [27] P.J. Jacques, Q. Furnémont, F. Lani, T. Pardoën, F. Delannay, Multiscale mechanics of
804 TRIP-assisted multiphase steels: I. Characterization and mechanical testing, *Acta Mater.*
805 55 (2007) 3681–3693. <https://doi.org/10.1016/j.actamat.2007.02.029>.
- 806 [28] M.C. Taboada, M.R. Elizalde, D. Jorge-Badiola, Austempering in low-C steels:
807 microstructure development and nanohardness characterization, *J. Mater. Sci.* 54 (2019)
808 5044–5060. <https://doi.org/10.1007/s10853-018-3159-6>.

- 809 [29] D. Raabe, B. Sun, A. Kwiatkowski Da Silva, B. Gault, H.W. Yen, K. Sedighiani, P.
810 Thoudden Sukumar, I.R. Souza Filho, S. Katnagallu, E. Jägle, P. Kürnsteiner, N.
811 Kusampudi, L. Stephenson, M. Herbig, C.H. Liebscher, H. Springer, S. Zaefferer, V.
812 Shah, S.L. Wong, C. Baron, M. Diehl, F. Roters, D. Ponge, Current Challenges and
813 Opportunities in Microstructure-Related Properties of Advanced High-Strength Steels,
814 Metall. Mater. Trans. A Phys. Metall. Mater. Sci. 51 (2020) 5517–5586.
815 <https://doi.org/10.1007/s11661-020-05947-2>.
- 816 [30] R. Cao, J. Li, D.S. Liu, J.Y. Ma, J.H. Chen, Micromechanism of Decrease of Impact
817 Toughness in Coarse-Grain Heat-Affected Zone of HSLA Steel with Increasing
818 Welding Heat Input, Metall. Mater. Trans. A Phys. Metall. Mater. Sci. 46 (2015) 2999–
819 3014. <https://doi.org/10.1007/s11661-015-2916-2>.
- 820 [31] J. Chakraborty, P.P. Chattopadhyay, D. Bhattacharjee, I. Manna, Microstructural
821 refinement of bainite and martensite for enhanced strength and toughness in high-carbon
822 low-alloy steel, Metall. Mater. Trans. A Phys. Metall. Mater. Sci. 41 (2010) 2871–2879.
823 <https://doi.org/10.1007/s11661-010-0288-1>.
- 824 [32] J. Cui, W. Zhu, Z. Chen, L. Chen, Microstructural Characteristics and Impact Fracture
825 Behaviors of a Novel High-Strength Low-Carbon Bainitic Steel with Different Reheated
826 Coarse-Grained Heat-Affected Zones, Metall. Mater. Trans. A Phys. Metall. Mater. Sci.
827 51 (2020) 6258–6268. <https://doi.org/10.1007/s11661-020-06017-3>.
- 828 [33] D. Liu, M. Luo, B. Cheng, R. Cao, J. Chen, Microstructural Evolution and Ductile-to-
829 Brittle Transition in a Low-Carbon MnCrMoNiCu Heavy Plate Steel, Metall. Mater.
830 Trans. A Phys. Metall. Mater. Sci. 49 (2018) 4918–4936.
831 <https://doi.org/10.1007/s11661-018-4823-9>.
- 832 [34] T. Jia, Y. Zhou, X. Jia, Z. Wang, Effects of Microstructure on CVN Impact Toughness
833 in Thermomechanically Processed High Strength Microalloyed Steel, Metall. Mater.
834 Trans. A Phys. Metall. Mater. Sci. 48 (2017) 685–696. <https://doi.org/10.1007/s11661-016-3893-9>.
- 836 [35] G. Gao, B. An, H. Zhang, H. Guo, X. Gui, B. Bai, Concurrent enhancement of ductility
837 and toughness in an ultrahigh strength lean alloy steel treated by bainite-based
838 quenching-partitioning-tempering process, Mater. Sci. Eng. A. 702 (2017) 104–112.
839 <https://doi.org/10.1016/j.msea.2017.05.087>.
- 840 [36] X. Di, M. Tong, C. Li, C. Zhao, D. Wang, Microstructural evolution and its influence
841 on toughness in simulated inter-critical heat affected zone of large thickness bainitic
842 steel, Mater. Sci. Eng. A. 743 (2019) 67–76.
843 <https://doi.org/10.1016/j.msea.2018.11.070>.
- 844 [37] F.G. Caballero, H. Roelofs, S. Hasler, C. Capdevila, J. Chao, J. Cornide, C. Garcia-
845 Mateo, Influence of bainite morphology on impact toughness of continuously cooled
846 cementite free bainitic steels, Mater. Sci. Technol. 28 (2012) 95–102.
847 <https://doi.org/10.1179/1743284710Y.0000000047>.
- 848 [38] S. Pallaspuro, A. Kaijalainen, S. Mehtonen, J. Kömi, Z. Zhang, D. Porter, Effect of
849 microstructure on the impact toughness transition temperature of direct-quenched steels,
850 Mater. Sci. Eng. A. 712 (2018) 671–680. <https://doi.org/10.1016/j.msea.2017.12.037>.
- 851 [39] R. Cao, Z. Yang, Z. Chan, W. Lei, J. Li, J. Zhang, X. Liang, J. Chen, The determination
852 of the weakest zone and the effects of the weakest zone on the impact toughness of the
853 12Cr2Mo1R welded joint, J. Manuf. Process. 50 (2020) 539–546.
854 <https://doi.org/10.1016/j.jmapro.2020.01.014>.
- 855 [40] S.Y. Han, S.Y. Shin, S. Lee, N.J. Kim, J.H. Bae, K. Kim, Effects of cooling conditions
856 on tensile and charpy impact properties of API X80 linepipe steels, Metall. Mater. Trans.
857 A Phys. Metall. Mater. Sci. 41 (2010) 329–340. <https://doi.org/10.1007/s11661-009-0135-4>.

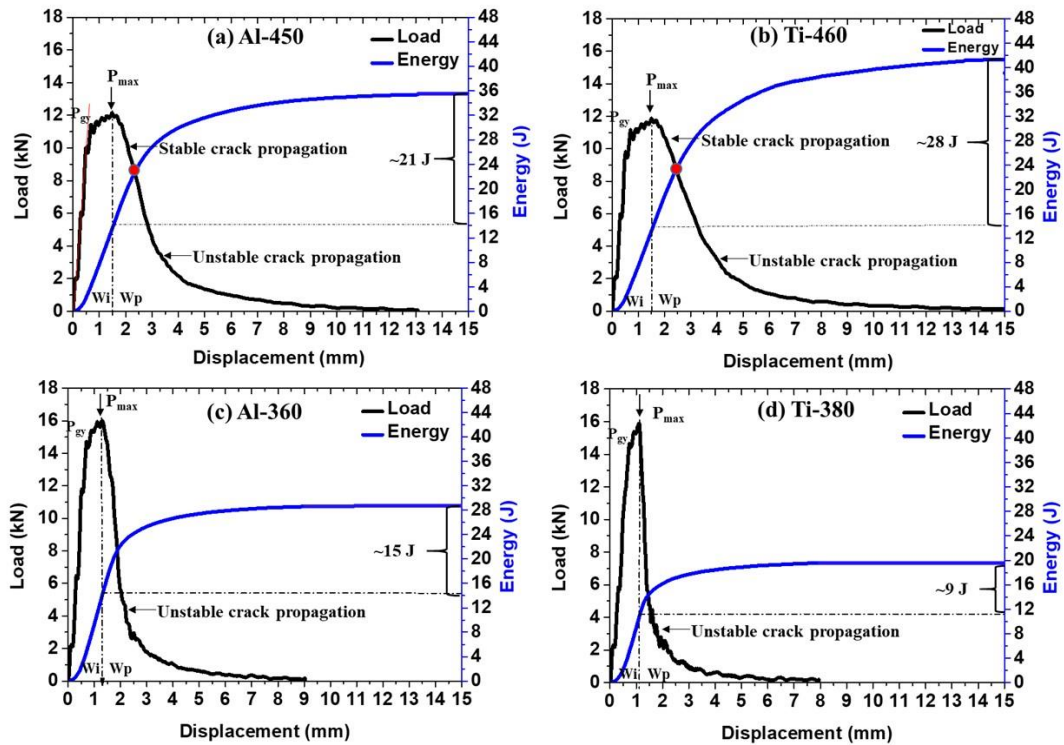
- 859 [41] G. Liang, Q. Tan, Y. Liu, T. Wu, X. Yang, Z. Tian, A. Atrens, M.X. Zhang, Effect of
860 cooling rate on microstructure and mechanical properties of a low-carbon low-alloy
861 steel, *J. Mater. Sci.* 56 (2021) 3995–4005. <https://doi.org/10.1007/s10853-020-05483-9>.
- 862 [42] H.K. Sung, S.Y. Shin, B. Hwang, C.G. Lee, N.J. Kim, S. Lee, Effects of rolling and
863 cooling conditions on microstructure and tensile and Charpy impact properties of ultra-
864 low-carbon high-strength bainitic steels, *Metall. Mater. Trans. A Phys. Metall. Mater.*
865 *Sci.* 42 (2011) 1827–1835. <https://doi.org/10.1007/s11661-010-0590-y>.
- 866 [43] H.K. Sung, S.Y. Shin, B. Hwang, C.G. Lee, S. Lee, Effects of cooling conditions on
867 microstructure, tensile properties, and charpy impact toughness of low-carbon high-
868 strength bainitic steels, *Metall. Mater. Trans. A Phys. Metall. Mater. Sci.* 44 (2013) 294–
869 302. <https://doi.org/10.1007/s11661-012-1372-5>.
- 870 [44] H. Terasaki, Y. Shintome, Y. ichi Komizo, M. Ohata, K. Moriguchi, Y. Tomio, Effect
871 of Close-Packed Plane Boundaries in a Bain Zone on the Crack Path in Simulated
872 Coarse-Grained HAZ of Bainitic Steel, *Metall. Mater. Trans. A Phys. Metall. Mater.*
873 *Sci.* 46 (2015) 2035–2039. <https://doi.org/10.1007/s11661-015-2817-4>.
- 874 [45] Z. Zhu, J. Han, H. Li, Influence of Heat Input on Microstructure and Toughness
875 Properties in Simulated CGHAZ of X80 Steel Manufactured Using High-Temperature
876 Processing, *Metall. Mater. Trans. A Phys. Metall. Mater. Sci.* 46 (2015) 5467–5475.
877 <https://doi.org/10.1007/s11661-015-3122-y>.
- 878 [46] H.K.D.H. Bhadeshia, Bainite in Steels, CRC Press, 2019.
879 <https://doi.org/10.1201/9781315096674>.
- 880 [47] Y. Tomita, K. Okabayashi, Heat treatment for improvement in lower temperature
881 mechanical properties of 0.40 pct C-Cr-Mo ultrahigh strength steel, *Metall. Mater. Trans. A* 14
882 (1983) 2387–2393. <https://doi.org/10.1007/BF02663314>.
- 883 [48] T.V.L.N. Rao, S.N. Dikshit, G. Malakondaiah, P.R. Rao, On mixed upper bainite-
884 martensite in an AISI 4330 steel exhibiting an uncommonly improved strength-
885 toughness combination, *Scr. Metall. Mater.* 24 (1990) 1323–1328.
886 [https://doi.org/10.1016/0956-716X\(90\)90350-P](https://doi.org/10.1016/0956-716X(90)90350-P).
- 887 [49] J. Hu, L.X. Du, J.J. Wang, Q.Y. Sun, Cooling process and mechanical properties design
888 of hot-rolled low carbon high strength microalloyed steel for automotive wheel usage,
889 *Mater. Des.* 53 (2014) 332–337. <https://doi.org/10.1016/j.matdes.2013.07.036>.
- 890 [50] W. Zhao, W. Wang, S. Chen, J. Qu, Effect of simulated welding thermal cycle on
891 microstructure and mechanical properties of X90 pipeline steel, *Mater. Sci. Eng. A* 528
892 (2011) 7417–7422. <https://doi.org/10.1016/j.msea.2011.06.046>.
- 893 [51] Z. Zhu, J. Han, H. Li, C. Lu, High temperature processed high Nb X80 steel with
894 excellent heat-affected zone toughness, *Mater. Lett.* 163 (2016) 171–174.
895 <https://doi.org/10.1016/j.matlet.2015.10.071>.
- 896 [52] B. Hwang, C.G. Lee, Influence of thermomechanical processing and heat treatments on
897 tensile and Charpy impact properties of B and Cu bearing high-strength low-alloy steels,
898 *Mater. Sci. Eng. A* 527 (2010) 4341–4346. <https://doi.org/10.1016/j.msea.2010.03.106>.
- 899 [53] H.K. Sung, S.Y. Shin, B. Hwang, C.G. Lee, S. Lee, Effects of B and Cu addition and
900 cooling rate on microstructure and mechanical properties in low-carbon, high-strength
901 bainitic steels, *Metall. Mater. Trans. A Phys. Metall. Mater. Sci.* 43 (2012) 3703–3714.
902 <https://doi.org/10.1007/s11661-012-1183-8>.
- 903 [54] H.K. Sung, S. Lee, S.Y. Shin, Effects of start and finish cooling temperatures on
904 microstructure and mechanical properties of low-carbon high-strength and low-yield
905 ratio bainitic steels, in: *Metall. Mater. Trans. A Phys. Metall. Mater. Sci.*, Springer
906 Boston, 2014: pp. 2004–2013. <https://doi.org/10.1007/s11661-013-2156-2>.
- 907 [55] S.K. Dhua, P.P. Sarkar, A. Saxena, B.K. Jha, Development of Fine-Grained, Low-
908 Carbon Bainitic Steels with High Strength and Toughness Produced Through the

- 909 Conventional Hot-Rolling and Air-Cooling, Metall. Mater. Trans. A Phys. Metall.
910 Mater. Sci. 47 (2016) 6224–6236. <https://doi.org/10.1007/s11661-016-3720-3>.
- 911 [56] F. Boratto, R. Barbosa, S. Yue, J.J. Jonas, Effect of chemical composition on the critical
912 temperature of microalloyed steels, in: THERMEC' 88, 1988: pp. 383–390.
- 913 [57] (CEN) European Committee for Standardisation, BS EN 10025-1:2004 Hot rolled
914 products of structural steels. General technical delivery conditions, (2004) 36.
915 <https://www.en-standard.eu/set-bs-en-10025-2-6-2019-hot-rolled-products-of-structural-steels/> (accessed July 7, 2021).
- 916 [58] ASTM Int., ASTM E8/E8M - Standard Test Methods for Tension Testing of Metallic
917 Materials, ASTM Int. (2016) 1–27. https://doi.org/10.1520/E0008_E0008M-16A.
- 918 [59] ASTM International, ASTM E23 – 18, Standard Test Methods for Notched Bar Impact
919 Testing of Metallic Materials, ASTM Int. (2018) 1–26.
920 <https://www.astm.org/Standards/E23> (accessed April 24, 2021).
- 921 [60] Y. Sakai, K. Tamanoi, N. Ogura, Application of tanh curve fit analysis to fracture
922 toughness data of Japanese RPVS, Nucl. Eng. Des. 115 (1989) 31–39.
923 [https://doi.org/10.1016/0029-5493\(89\)90257-4](https://doi.org/10.1016/0029-5493(89)90257-4).
- 924 [61] A. Ghosh, A. Ray, D. Chakrabarti, C.L. Davis, Cleavage initiation in steel: Competition
925 between large grains and large particles, Mater. Sci. Eng. A. 561 (2013) 126–135.
926 <https://doi.org/10.1016/j.msea.2012.11.019>.
- 927 [62] Z. Cong, Y. Murata, Dislocation Density of Lath Martensite in 10Cr-5W Heat-Resistant
928 Steels, Mater. Trans. 52 (2011) 2151–2154.
929 <https://doi.org/10.2320/matertrans.M2011201>.
- 930 [63] F. HajyAkbari, J. Sietsma, A.J. Böttger, M.J. Santofimia, An improved X-ray
931 diffraction analysis method to characterize dislocation density in lath martensitic
932 structures, Mater. Sci. Eng. A. 639 (2015) 208–218.
933 <https://doi.org/10.1016/j.msea.2015.05.003>.
- 934 [64] K. Venkateswarlu, M. Sandhyarani, T.A. Nellaippan, N. Rameshbabu, Estimation of
935 Crystallite Size, Lattice Strain and Dislocation Density of Nanocrystalline Carbonate
936 Substituted Hydroxyapatite by X-ray Peak Variance Analysis, Procedia Mater. Sci. 5
937 (2014) 212–221. <https://doi.org/10.1016/J.MSPRO.2014.07.260>.
- 938 [65] G.K. Williamson, R.E. Smallman, III. Dislocation densities in some annealed and cold-
939 worked metals from measurements on the X-ray debye-scherrer spectrum, Philos. Mag.
940 1 (1956) 34–46. <https://doi.org/10.1080/14786435608238074>.
- 941 [66] P. Lehto, Adaptive domain misorientation approach for the EBSD measurement of
942 deformation induced dislocation sub-structures, Ultramicroscopy. 222 (2021) 113203.
943 <https://doi.org/10.1016/j.ultramic.2021.113203>.
- 944 [67] C. Moussa, M. Bernacki, R. Besnard, N. Bozzolo, Statistical analysis of dislocations and
945 dislocation boundaries from EBSD data, Ultramicroscopy. 179 (2017) 63–72.
946 <https://doi.org/10.1016/j.ultramic.2017.04.005>.
- 947 [68] J. Zhao, W. Hu, X. Wang, J. Kang, Y. Cao, G. Yuan, H. Di, R.D.K. Misra, A Novel
948 thermo-mechanical controlled processing for large-thickness microalloyed 560 MPa
949 (X80) pipeline strip under ultra-fast cooling, Mater. Sci. Eng. A. 673 (2016) 373–377.
950 <https://doi.org/10.1016/J.MSEA.2016.07.089>.
- 951 [69] W.C. Oliver, G.M. Pharr, An improved technique for determining hardness and elastic
952 modulus using load and displacement sensing indentation experiments, J. Mater. Res. 7
953 (1992) 1564–1583. <https://doi.org/10.1557/jmr.1992.1564>.
- 954 [70] G. Hou, F. Wang, K. Xu, Extracting yield strength and strain-hardening exponent of
955 metals with a double-angle indenter, J. Mater. Res. 24 (2009) 1674–1682.
956 <https://doi.org/10.1557/jmr.2009.0203>.
- 957 [71] B.W. Choi, D.H. Seo, J. Il Jang, A nanoindentation study on the micromechanical

- characteristics of API X100 pipeline steel, *Met. Mater. Int.* 15 (2009) 373–378. <https://doi.org/10.1007/s12540-009-0373-4>.
- [72] H. Azizi, H.S. Zurob, D. Embury, X. Wang, K. Wang, B. Bose, Using architectured materials to control localized shear fracture, *Acta Mater.* 143 (2018) 298–305. <https://doi.org/10.1016/j.actamat.2017.10.027>.
- [73] A. Karimzadeh, S.S. R. Koloor, M.R. Ayatollahi, A.R. Bushroa, M.Y. Yahya, Assessment of Nano-Indentation Method in Mechanical Characterization of Heterogeneous Nanocomposite Materials Using Experimental and Computational Approaches, *Sci. Rep.* 9 (2019) 1–14. <https://doi.org/10.1038/s41598-019-51904-4>.
- [74] L. Lu, M. Dao, P. Kumar, U. Ramamurty, G.E. Karniadakis, S. Suresh, Extraction of mechanical properties of materials through deep learning from instrumented indentation, *Proc. Natl. Acad. Sci. U. S. A.* 117 (2020) 7052–7062. <https://doi.org/10.1073/pnas.1922210117>.
- [75] K.K. Tho, S. Swaddiwudhipong, Z.S. Liu, K. Zeng, Simulation of instrumented indentation and material characterization, *Mater. Sci. Eng. A.* 390 (2005) 202–209. <https://doi.org/10.1016/j.msea.2004.08.037>.
- [76] M. Dao, N. Chollacoop, K.J. Van Vliet, T.A. Venkatesh, S. Suresh, Computational modeling of the forward and reverse problems in instrumented sharp indentation, *Acta Mater.* 49 (2001) 3899–3918. [https://doi.org/10.1016/S1359-6454\(01\)00295-6](https://doi.org/10.1016/S1359-6454(01)00295-6).
- [77] J.L. Bucaille, S. Stauss, E. Felder, J. Michler, Determination of plastic properties of metals by instrumented indentation using different sharp indenters, *Acta Mater.* 51 (2003) 1663–1678. [https://doi.org/10.1016/S1359-6454\(02\)00568-2](https://doi.org/10.1016/S1359-6454(02)00568-2).
- [78] A.E. Giannakopoulos, S. Suresh, Determination of elastoplastic properties by instrumented sharp indentation, *Scr. Mater.* 40 (1999) 1191–1198. [https://doi.org/10.1016/S1359-6462\(99\)00011-1](https://doi.org/10.1016/S1359-6462(99)00011-1).
- [79] R.W. Hertzberg, R.P. Vinci, J.L. Hertzberg, Deformation and Fracture Mechanics of Engineering Materials (2nd Edition), 2020. <https://doi.org/10.1111/1.3264456>.
- [80] H.-J. Schindler, Relation Between Fracture Toughness and Charpy Fracture Energy: An Analytical Approach, in: Pendul. Impact Test. A Century Prog., ASTM International, 100 Barr Harbor Drive, PO Box C700, West Conshohocken, PA 19428-2959, 2000: pp. 337–337–17. <https://doi.org/10.1520/STP14405S>.
- [81] H.J. Schindler, Estimation of the Dynamic J-R curve from a Single Impact Bending Test, in: Proc. 11th Eur. Conf. Fract., 1996: pp. 2007–2012. <https://www.dora.lib4ri.ch/empa/islandora/object/empa%3A11211/> (accessed April 4, 2021).
- [82] W.L. Server, IMPACT THREE-POINT BEND TESTING FOR NOTCHED AND PRECRACKED SPECIMENS., *J. Test. Eval.* 6 (1978) 29–34. <https://doi.org/10.1520/jte10915j>.
- [83] A. Moitra, P.R. Sreenivasan, P. Parameswaran, S.L. Mannan, Dynamic deformation and fracture properties of simulated weld heat affected zone of 9Cr-1Mo steel from instrumented impact tests, *Mater. Sci. Technol.* 18 (2003) 1195–1200. <https://doi.org/10.1179/026708302225006106>.
- [84] Z. Yue, Y. Zhu, J. Fan, Z. Shao, The strain rate sensitivity exponent and the strain hardening exponent of as-cast TC21 titanium alloy in β single-phase region, *Mater. Res. Express.* 6 (2019). <https://doi.org/10.1088/2053-1591/ab513f>.
- [85] A. Chatterjee, A. Moitra, A.K. Bhaduri, R. Mitra, D. Chakrabarti, Dynamic fracture behaviour of thermo-mechanically processed modified 9Cr-1Mo steel, *Eng. Fract. Mech.* 149 (2015) 74–88. <https://doi.org/10.1016/j.engfracmech.2015.09.051>.
- [86] J. Barsom, S. Rolfe, Correlations Between K_{Ic} and Charpy V-Notch Test Results in the Transition-Temperature Range, in: Impact Test. Met., ASTM International, 100 Barr

- 1009 Harbor Drive, PO Box C700, West Conshohocken, PA 19428-2959, 2009: pp. 281–281–
1010 22. <https://doi.org/10.1520/stp32067s>.
- 1011 [87] Y. Tanaka, T. Iwadate, K. Suzuki, Small specimen measurements of dynamic fracture
1012 toughness of heavy section steels for nuclear reactor pressure vessels, *Int. J. Press.*
1013 *Vessel. Pip.* 31 (1988) 221–236. [https://doi.org/10.1016/0308-0161\(88\)90004-X](https://doi.org/10.1016/0308-0161(88)90004-X).
- 1014 [88] J.R. Rice, D.M. Tracey, On the ductile enlargement of voids in triaxial stress fields*, *J.*
1015 *Mech. Phys. Solids.* 17 (1969) 201–217. [https://doi.org/10.1016/0022-5096\(69\)90033-7](https://doi.org/10.1016/0022-5096(69)90033-7).
- 1017 [89] F.A. McClintock, Local criteria for ductile fracture, *Int. J. Fract. Mech.* 4 (1968) 101–
1018 130. <https://doi.org/10.1007/BF00188939>.
- 1019 [90] A. Karmakar, S. Sivaprasad, S. Kundu, D. Chakrabarti, Tensile behavior of ferrite-
1020 carbide and ferrite-martensite steels with different ferrite grain structures, in: *Metall.*
1021 *Mater. Trans. A Phys. Metall. Mater. Sci.*, 2014: pp. 1659–1664.
1022 <https://doi.org/10.1007/s11661-014-2228-y>.
- 1023 [91] J. Thornby, D. Verma, R. Cochrane, A. Westwood, V.B. Manakari, M. Gupta, M.
1024 Haghshenas, Indentation-based characterization of creep and hardness behavior of
1025 magnesium carbon nanotube nanocomposites at room temperature, *SN Appl. Sci.* 2019
1026 17. 1 (2019) 1–12. <https://doi.org/10.1007/S42452-019-0696-9>.
- 1027 [92] S.I. Shakil, C. Dharmendra, B.S. Amirkhiz, D. Verma, M. Mohammadi, M. Haghshenas,
1028 Micromechanical characterization of wire-arc additive manufactured and cast nickel
1029 aluminum bronze: Ambient and intermediate temperatures, *Mater. Sci. Eng. A.* 792
1030 (2020) 139773. <https://doi.org/10.1016/J.MSEA.2020.139773>.
- 1031 [93] J.Y. Kim, K.W. Lee, J.S. Lee, D. Kwon, Determination of tensile properties by
1032 instrumented indentation technique: Representative stress and strain approach, *Surf.*
1033 *Coatings Technol.* 201 (2006) 4278–4283.
1034 <https://doi.org/10.1016/J.SURFCOAT.2006.08.054>.
- 1035 [94] M. Yetna N'Jock, D. Chicot, X. Decoopman, J. Lesage, J.M. Ndjaka, A. Pertuz,
1036 Mechanical tensile properties by spherical macroindentation using an indentation strain-
1037 hardening exponent, *Int. J. Mech. Sci.* 75 (2013) 257–264.
1038 <https://doi.org/10.1016/J.IJMECSCI.2013.07.008>.
- 1039 [95] D. Bhattacharjee, J.F. Knott, C.L. Davis, Charpy-Impact-Toughness Prediction using an
1040 “Effective” Grain Size for Thermomechanically Controlled Rolled Microalloyed Steels,
1041 *Metall. Mater. Trans. A Phys. Metall. Mater. Sci.* 35 A (2004) 121–130.
1042 <https://doi.org/10.1007/s11661-004-0115-7>.
- 1043 [96] A.S. Argon, Brittle to ductile transition in cleavage fracture, *Acta Metall.* 35 (1987) 185–
1044 196. [https://doi.org/10.1016/0001-6160\(87\)90228-8](https://doi.org/10.1016/0001-6160(87)90228-8).
- 1045 [97] P.B. Hirsch, S.G. Roberts, Comment on the brittle-to-ductile transition: A cooperative
1046 dislocation generation instability; dislocation dynamics and the strain-rate dependence
1047 of the transition temperature, *Acta Mater.* 44 (1996) 2361–2371.
1048 [https://doi.org/10.1016/1359-6454\(95\)00363-0](https://doi.org/10.1016/1359-6454(95)00363-0).
- 1049
- 1050
- 1051
- 1052
- 1053
- 1054
- 1055

1056 APENDIX-I



1057

1058 Fig. A1: Load vs. displacement curves obtained from instrumented Charpy impact testing of
 1059 the specimens at +70°C. The crack propagation energy calculated from the load-displacement
 1060 curves are mentioned on the images.